IEEE Access
Multidisciplinary ⋮ Rapid Review ⋮ Open Access Journal

Received November 9, 2020, accepted December 1, 2020, date of publication December 9, 2020,
date of current version December 21, 2020.

Digital Object Identifier 10.1109/ACCESS.2020.3043411

Antlion Optimized Robust Control Approach for Micropositioning Trajectory Tracking Tasks

AMMAR AL-JODAH[1,2], (Graduate Student Member, IEEE), BIJAN SHIRINZADEH[1], (Member, IEEE), JOSHUA PINSKIER[1], (Member, IEEE), MOHAMMADALI GHAFARIAN[1], (Graduate Student Member, IEEE), TILOK KUMAR DAS[1], (Graduate Student Member, IEEE), YANLING TIAN[3], AND DAWEI ZHANG[4]

[1]Robotics and Mechatronics Research Laboratory (RMRL), Department of Mechanical and Aerospace Engineering, Monash University, Melbourne, VIC 3800, Australia
[2]Department of Control and Systems Engineering, University of Technology, Baghdad 10066, Iraq
[3]School of Engineering, University of Warwick, Coventry CV4 7AL, U.K.
[4]School of Mechanical Engineering, Tianjin University, Tianjin 300072, China

Corresponding author: Ammar Al-Jodah (ammar.al-jodah@monash.edu)

This work was supported in part by the Australian Research Council (ARC) Linkage Infrastructure, Equipment and Facilities (LIEF) grant and in part by the ARC Discovery grant.

ABSTRACT Planar 3-Degree of Freedom (3-DOF) micropositioning stages are widely adopted in many precision applications for their ability to provide in-plane rotation. However, their motion accuracy is adversely affected by cross-couplings, model uncertainty, and external disturbances. This work proposes an optimized robust control methodology based on disturbance estimation to address these issues. Systematic modeling of a 3-DOF precision micropositioning stage was utilized to develop a nonlinear disturbance observer-based sliding mode control methodology. This methodology can estimate and compensate the unavoidable cross-couplings between the major axes of motion. A stability analysis is conducted to prove the stability of the feedback system when the control approach is combined with the disturbance observer. A maximum bound on the tracking error is derived through finite-time analysis, and the parameters that affect this bound are identified. The antlion optimizer algorithm is used to optimize the control parameter based on the mean square error cost function to eliminate the requirement for manual tuning and to achieve the best attainable performance. The proposed control method is experimentally demonstrated to track complex trajectory with less tracking error than the classical sliding mode approach. The main contribution of this study is the improvement of the trajectory tracking accuracy in multi-DOF micropositioners using an optimized disturbance observer-based robust control technique.

INDEX TERMS Sliding mode, disturbance observer, metaheuristic optimization, antlion optimizer, micropositioning.

I. INTRODUCTION

Planar Three Degree of Freedom (3-DOF) micro/nanopositioning mechanisms are essential in fields requiring both translation and orientation correction. Orientation correction is necessary to align samples with apparatus in processes such as photolithography, manipulation under atomic force microscope, micro-assembly, and many more [1]–[3]. Compliant mechanisms (CM) are typically used in the design of micro/nanopositioning mechanisms as they offer several advantages such as monolithic configuration, compact structure, high precision, zero backlash, and no wear [4]–[6]. Compliant manipulators are designed such that flexible elements' deformation transforms loads into motions [7].

XY micromanipulators are another planar type mechanisms which have been extensively studied in the literature as they offer an extensive range of motion; a few examples can be referred to [8]–[11]. Improving rotational stiffness and the utilization of decoupling mechanisms are usually employed in those mechanisms to improve the motion range and reduce parasitic motions such as cross-coupling and in-plane rotation. Despite the popularity of decoupling mechanisms that are used within XY micropositioners, in practice, cross-coupling and in-plane rotation still occur in linear

The associate editor coordinating the review of this manuscript and approving it for publication was Jason Gu.

motions due to assembly and manufacturing errors. These induced errors severely degrade motion accuracy, and thus a rotational compensation is required. The extra DOF offered by the planar 3-DOF micro/nanopositioning mechanisms can easily be used for orientation correction and manipulation to overcome these issues [12].

Planar 3-DOF XYΘ mechanisms have coupled kinematics, which makes them inherently more challenging to control than the decoupled XY mechanisms. The strongly present cross-axis coupling in these mechanisms has a substantial impact on the positioning accuracy. Moreover, it can even cause actuator damage if it was large enough [13]. The adverse effect of coupling is not only limited to flexure-based mechanisms; it was found that it results in mechanical components damage and excessive wear in sliding parts in dual-driven gantry systems. This behaviour was investigated and resolved by synchronizing the motors motions using advanced synchronization control schemes proposed in [14], and [15]. In flexure-based mechanisms, several attempts were directed towards improving the mechanical design to tackle the cross-coupling issues. Serial kinematics was considered in [16] where the θ-axis was serially connected to a decoupled XY stage. Although this configuration decouples the axes and simplifies its control, it could result in nonhomogeneous dynamics. Moreover, the cascaded structure results in large inertia for the moving stage, which reduces the natural frequency, and hence the maximum attainable speed of the stage. Another attempt was made to decouple the x and y motions in [17] using a decoupling mechanism. However, these motions were still coupled with the θ motion, and the use of the decoupling mechanism resulted in limited rotational motion. Therefore research efforts were shifted towards resolving the cross-coupling issues by improving control strategies. Estimation and compensation of cross-coupling were utilized to improve the motion accuracy effectively.

The intrinsic cross-coupling in parallel mechanisms have been widely studied in the literature [13], [18]–[20], where it was handled as unintended motions which act as external disturbances [20]. Robust control techniques such as Sliding Mode Control (SMC) are used to reduce these disturbances. Moreover, SMC is adopted to guarantee a robust system against uncertainties and unmodeled dynamics [21], [22]. The control gain in SMC is typically set to be higher than the maximum bound of the expected disturbance to eliminate its effect. However, this approach results in high chattering phenomena, which is a major disadvantage of this type of control methods. Several studies have investigated chattering reduction through the use of disturbance observers [23]. Where in these methods, the demand on the control action is reduced and in turns alleviate the chattering. Active disturbance rejection strategy was proposed in [24] and integrated with backstepping and extended state observer to improve tracking control in nonlinear systems. The approach was applied to a robotic manipulator, and the results showed improved performance over traditional adaptive control methods. A linear disturbance observer was used in [25] along with an adaptive integral terminal third-order sliding-mode controller. The method was applied to a single-DOF mechanism to achieve high tracking performance with no chattering. Limited work has been done in the direction of disturbance observer-based control for XYΘ micro/nanopositioning mechanisms due to their actuation and sensing complexity. A control approach was proposed in [26] to regulate a 3-PRR XYΘ micropositioning mechanisms; however, as in [25], a linear observer was used. Another linear disturbance observer that utilized Extended State Observer (ESO) was proposed in [27] to control a VCM-based XYΘ micropositioning mechanism. However, ESOs are sensitive to the sampling rate. A high sampling rate is required to maintain high control performance, which sometimes is not feasible due to hardware limitations. Since XYΘ micropositioning mechanisms are highly coupled systems and inherently associated with non-linear cross-coupling, the utilization of linear observers may be unreliable.

Another issue that associated with the control of multi-DOF mechanisms is the plethora of the control parameters that need manual tuning to achieve the required performance. Manual tuning is not practical as it might risk the safety of the system by selecting unstable or highly-oscillatory parameter combinations. Moreover, the maximum attainable performance is not guaranteed. Therefore it is necessary to automate this process using an optimization algorithm.

Optimization algorithms are categorized into local and global search algorithms. Local search algorithms, especially the gradient-based ones, are having a high chance of trapping in local minima solutions, and their convergence is highly sensitive to initial values. In contrast, global search algorithms do not suffer from those disadvantages due to the derivative-free nature of those algorithms. Several global search algorithms have been proposed in the literature, such as Genetic Algorithm (GA) [28], Differential Evolution (DE) [29], Particle Swarm Optimization (PSO) [30], Spider Monkey Optimization (SMO) [31], and many others.

These algorithms try to locate the global optima of the optimization problem by deploying several search agents in the solution space. Those agents follow exploration and exploitation strategies to explore their surroundings and to find an optimal solution. These strategies are essential to avoid the local minima, which may result in a premature convergence in some algorithms. The Antlion Optimizer (ALO) proposed in [32], is one of these metaheuristic optimization algorithms that is inspired by the biological behaviour of antlions. It has a superior advantage over other algorithms as it utilizes global and local search for its exploration and exploitation phases. This combination leads to a better exploration of the search space and rapid convergence to the optimal solution. Hence, it has been adopted in this work for optimizing the control parameters. The local optima avoidance and simplicity of ALO have made it successful in solving several critical optimization problems [33]–[35].

Sliding mode control method optimization by metaheuristic methods has been investigated in several studies. A classical sliding mode control method with a boundary layer hyperbolic tangent function was proposed in [36] for tracking tasks in voltage source converter high voltage direct current (VSC-HVDC) transmission systems. Classical Modified Genetic Algorithm (MGA) and PSO were utilized to optimize the controller gains. However, the use of the tangent function will cause the tracking error to approach a maximum bound. This bound was not investigated, and the parameters that affect it were not identified. In [37], a sliding mode control was combined with a linear quadratic regulator for trajectory tracking of a helicopter system. The control gains were optimized using metaheuristic algorithms. The total variance of the control signal was used in the objective function to overcome the chattering issue. However, that increased the tracking error because of the trade-off nature of the selected objective function. Moreover, the control signal exhibited large chattering due to the direct use of the signum function. A similar issue was observed in [38], where the objective function was based on a trade-off between chattering reduction and tracking error, which resulted in high chattering in the control signal. Apart from these studies, the vast majority of the literature used try and error approach for selecting sliding mode control parameters, which introduces issues with suboptimal tracking and high chattering of the control signal.

Based on what has been discussed, it can be summarized that linear disturbance observers and manual tuning methods are not practical to reduce cross-coupling and achieve optimal performance in XYΘ micropositioners. Moreover, the bound of the tracking error in sliding mode control should be identified when chattering attenuation methods are used, and this bound should be reduced to its optimal feasible value. Thus, these factors should be considered and investigated in more reliable control approaches. The contributions of this work can be summarized as:

- A disturbance observer-based sliding mode control method is proposed for tracking tasks in micropositioning systems with optimized gains to reduce error bound.
- Nonlinear disturbance observer is utilized to reduce the demand on the switching control gain to be just higher than the disturbance estimation error. Thus, that reduces the chattering effect on the system.
- The time convergence analysis of the robust control method is investigated, and the error is proved to be confined within a maximum bound ρ, which can be reduced by designing the control parameters.
- The parameters that affect his bound are identified and optimized in a metaheuristic optimization approach to maximize the tracking ability of the micropositioning system, and to overcome the chattering issues.

In this work, a sliding mode control scheme based on a nonlinear disturbance observer is proposed to handle trajectory tracking tasks in XYΘ micropositioning mechanisms. This methodology can estimate and compensate the unavoidable cross-couplings and reduce chattering pneumonia, as these two represent significant disadvantages in such mechanisms. The control parameters are obtained by the antlion optimizer to achieve optimal performance and to reduce the demand for manual tuning. The time convergence and stability analyses are undertaken when this control methodology. Furthermore, The experimental and simulation results confirm the stability, robustness, and effectiveness of the proposed control method in reducing cross-coupling effects and improving the tracking performance in micropositioning systems.

II. MECHANISM MODELING AND IDENTIFICATION

The planar micropositioning mechanism used in this work is shown in Fig. 1. It provides two translation and one rotation. The mechanism consists of threefold rotational symmetry, where three driving mechanisms are connected to the central platform in parallel, as shown in Fig. 1c. Each driving mechanism is composed of three flexure based joints connected in series to produce a 3-DOF motion. The first joint provides an active prismatic motion in the horizontal direction, while the second joint offers a passive vertical prismatic motion, and finally, the third one yields a passive rotation. Voice Coil Motors (VCMs) induce movements in the links. Wire electric discharge machining was used to fabricate a monolithic mechanism, where Aluminum 7075-T6 was used for its reliability. The motions are measured through three heterodyne laser interferometers to track displacement and rotation in realtime with high accuracy. Retroreflectors and external mirrors were used to reflect the laser beams to the interferometers and compensate for misalignment. The laser displacements are converted into platform displacements in realtime and feed into the control approach for control action calculations. The cross-coupling between the axis of this micropositioning mechanism poses challenges for tradition control techniques. Thus an advance control method that estimates and compensates these uncertainties is necessary.

A. SYSTEM MODELING

Flexure based micropositioners are ideally modeled as a damped mass where the platform represented as a lumped mass, and each flexure acts as a spring [39]. Therefore, three damped mass systems can model the mechanism in this work where each system corresponds to a degree of freedom. The overall system dynamics can be described by

$$M\ddot{\Upsilon} + C\dot{\Upsilon} + K\Upsilon = F \tag{1}$$

where Υ is the displacement vector and it is given by $\Upsilon = [x,\ y,\ \theta]^T$. Mass, stiffness, and damping coefficients are described by the diagonal matrices $M = diag(m_x,\ m_y,\ I_\theta)$, $\mathbf{K} = diag(k_x,\ k_y,\ k_\theta)$, and $\mathbf{C} = diag(c_x,\ c_y,\ c_\theta)$, respectively. Finally, F is the forces and moment vector and it is given by $\mathbf{F} = \left[f_x,\ f_y,\ M_z\right]$. This vector is related to the VCMs forces by

$$\mathbf{F} = \mathbf{J}^{-1^T}\ [f_{VCM1},\ f_{VCM2},\ f_{VCM3}]^T \tag{2}$$

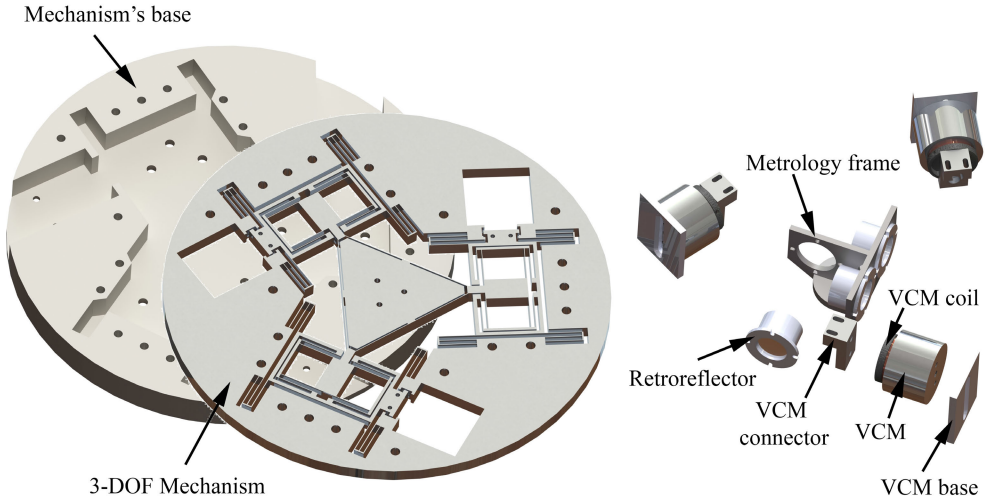

(a) Exploded view

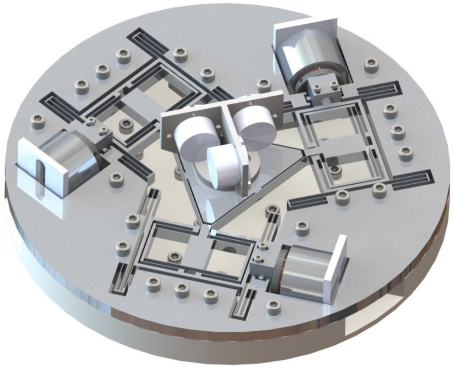

(b) Assembled view

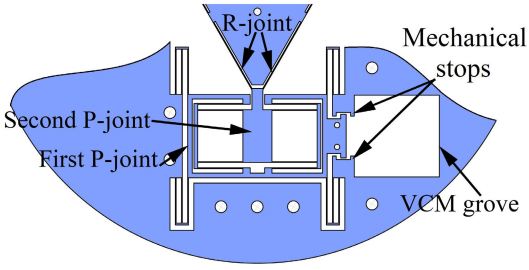

(c) Driving arm

FIGURE 1. The 3-DOF micropositioning system.

where $\mathbf{J}^{-1}$ is the inverse kinematics matrix and it is given by [40]

$$\mathbf{J}^{-1} = \begin{bmatrix} 1 & 0 & r \\ -1/2 & \sqrt{3}/2 & r \\ -1/2 & -\sqrt{3}/2 & r \end{bmatrix} \tag{3}$$

where r is radius of the circumference circle of the stage. The generated force of the VCM is a combination of coil force *fcoil* and electrical disturbances and noise lumped into a parameter d as follows

$$f_{VCM_j} = fcoil_j + d_j(t), \quad j = 1 - 3 \tag{4}$$

The overall system can be found from Eqs. (1 - 4) as follows

$$\ddot{\Upsilon} = -\mathbf{C}'\dot{\Upsilon} - \mathbf{K}'\Upsilon + \mathbf{M}'\mathbf{J}^{-1^T}\left(\mathbf{f}^T + \mathbf{d}^T\right) \tag{5}$$

where $\mathbf{C}' = diag(\frac{c_x}{m_x}, \frac{c_y}{m_y}, \frac{c_\theta}{I_\theta})$, $\mathbf{K}' = diag(\frac{k_x}{m_x}, \frac{k_y}{m_y}, \frac{k_\theta}{I_\theta})$, $\mathbf{M}' = diag(\frac{1}{m_x}, \frac{1}{m_y}, \frac{1}{I_\theta})$, $\mathbf{f} = [f_{coil1}, f_{coil2}, f_{coil3}]$, and $\mathbf{d} = \left[d_x, d_y, d_\theta\right]$.

Inverse kinematics is typically used to decouple the system, which facilitates the control of each axis separately [41], [42]. Although this decoupling approach is not perfect, it reduces the complexity of the control methodology. The residual cross-couplings are augmented with the disturbance vector under a lumped disturbance parameter. Based on this method, the dynamics of each axis of motion can be described by

$$(m_\upsilon + \triangle m_\upsilon)\,\ddot{\upsilon} + (c_\upsilon + \triangle c_\upsilon)\,\dot{\upsilon} + (k_\upsilon + \triangle k_\upsilon)\,\upsilon = u_\upsilon + \delta(t) \tag{6}$$

where υ represents a given axis (x, y, or θ); the control action is represented by u_υ; the parameter uncertainties are given by $\triangle m_\upsilon$, $\triangle c_\upsilon$, and $\triangle k_\upsilon$, and $\delta(t)$ represent external disturbances that may include cross-couplings, sensing noise, drivers noise, etc. Rearranging the above equation as

$$\ddot{\upsilon} = -\frac{c_\upsilon}{m_\upsilon}\dot{\upsilon} - \frac{k_\upsilon}{m_\upsilon}\upsilon + \frac{1}{m_\upsilon}u_\upsilon + \frac{1}{m_\upsilon}\left(\delta(t) - \triangle m_\upsilon\ddot{\upsilon} - \triangle c_\upsilon\dot{\upsilon} - \triangle k_\upsilon\upsilon\right) \tag{7}$$

which can be rewritten as

$$\ddot{\upsilon} = -\frac{c_\upsilon}{m_\upsilon}\dot{\upsilon} - \frac{k_\upsilon}{m_\upsilon}\upsilon + \frac{1}{m_\upsilon}(u_\upsilon + d_\upsilon) \tag{8}$$

TABLE 1. Estimated system parameters.

υ	Mass, Inertia (m_υ, I_θ)	Stiffness (k_υ) N/m	Damping (c_υ) Ns/m
x	0.0361 kg	1.3610e3	1.1854
y	0.0364 kg	1.3441e3	1.1751
θ	0.0204 kg.m^2	1.0648e3	2.0001

where d_υ is the lumped disturbance, and it is given by

$$d_\upsilon = \delta(t) - \triangle m_\upsilon \ddot{\upsilon} - \triangle c_\upsilon \dot{\upsilon} - \triangle k_\upsilon \upsilon \tag{9}$$

The dynamics Eq. (8) can be represented as a state space system as follows

$$\begin{bmatrix} \dot{\upsilon}_1 \\ \dot{\upsilon}_2 \end{bmatrix} = \begin{bmatrix} 0 & 1 \\ -\dfrac{k_\upsilon}{m_\upsilon} & -\dfrac{c_\upsilon}{m_\upsilon} \end{bmatrix} \begin{bmatrix} \upsilon_1 \\ \upsilon_2 \end{bmatrix} + \begin{bmatrix} 0 \\ \dfrac{1}{m_\upsilon} \end{bmatrix} (u_\upsilon + d_\upsilon) \tag{10}$$

where $\upsilon_1 = \upsilon$ and $\upsilon_2 = \dot{\upsilon}$.

B. SYSTEM IDENTIFICATION

The system dynamics were experimentally identified using the nonlinear least-squares method. A 0.1 V amplitude sinusoidal signal with a frequency spectrum from 1-1000 Hz, and a sampling frequency of 10 kHz was used in open loop, to excite the system modes. The inverse kinematics was used to utilize the excitation of each axis separately. The system dynamics model is given by

$$\begin{bmatrix} X(s) \\ Y(s) \\ \Theta(s) \end{bmatrix} = \begin{bmatrix} G_{x1}(s) & G_{x2}(s) & G_{x3}(s) \\ G_{y1}(s) & G_{y2}(s) & G_{y3}(s) \\ G_{\theta 1}(s) & G_{\theta 2}(s) & G_{\theta 3}(s) \end{bmatrix} \begin{bmatrix} U_1(s) \\ U_2(s) \\ U_3(s) \end{bmatrix} \tag{11}$$

where $G_{x1}(s)$, $G_{y2}(s)$, and $G_{\theta 3}(s)$ are the intended motions transfer functions, and the rest are cross-coupling transfer functions, and $U_1(s)$, $U_2(s)$, and $U_3(s)$ represent the components of Eq. (2). Second order models were selected for the transfer functions in Eq. 11, because they sufficiently represent the dynamics of the micropositioning stage as evident from the experimental and estimated frequency responses shown in Fig. 2. The numerical values of Eq. 11 are given in Appendix A. The system parameters for the intended motions were found based on $G_{x1}(s)$, $G_{y2}(s)$, and $G_{\theta 3}(s)$, and they are presented in Table 1.

III. CONTROL METHOD DESIGN

The decoupling through inverse kinematics utilized in the open-loop scheme enabled the modeling of this 3-DOF mechanism into three separate systems. Thus each axis can be controlled as an independent system. However, due to manufacturing errors, motor driver noise and disturbances, this decoupling approach will suffer from some residual cross-coupling in each axis which affects the motion accuracy. Hence, it is necessary to reduce its adverse effect. The control method proposed here will handle residual cross-coupling, uncertainty in parameters, and disturbances as a lumped disturbance induced in each axis, and it will try to estimate and compensate its effect. A nonlinear disturbance observer was used for estimating lumped disturbances present in each axis of motion. This observer is then augmented with the sliding mode control approach to improve motion accuracy. The state-space model in Eq. (10) is used for the control methodology development.

A. SLIDING MODE CONTROL DESIGN

The design of sliding mode control involves the design of the sliding surface, and the reaching control law [43]. The system dynamics will be reduced to the sliding surface dynamics in the sliding mode control method [44]. Thus the control system specification should be considered when designing this surface. Since tracking performance is essential in micro/nanopositioning, a sliding surface that contains an integral action is necessary. A PID surface was used in this work to serve this purpose. The control action is developed accordingly to bring the system trajectories towards the surface using a switching control action. Once the trajectories reached the surface, they should be confined within a boundary of the sliding function and asymptomatically approach the origin. The sliding surface is selected as

$$s(t) = k_d \dot{e}(t) + k_p e(t) + k_i \int_0^t e(\tau) d\tau \tag{12}$$

where k_d, k_p, and k_i are the PID coefficients, and $e(t)$ is the trajectory tracking error signal. Henceforth, the time parameter (t) will be dropped for brevity. The error is described by

$$e = \upsilon_1 - \upsilon_{1des} \tag{13}$$

where υ_{1des} is the desired signal. The control action u_υ consists of the equivalent control u_{eq}, and the switching control u_{sw}, as follows

$$u_\upsilon = u_{eq} + u_{sw} \tag{14}$$

The systems trajectories are maintained within the sliding manifold by the equivalent control, while they are driven towards that manifold through the switching control [45]. The trajectories are successfully maintained within the sliding surface when the sliding condition, given by Eq. (15), is satisfied.

$$\dot{s} = 0 \tag{15}$$

For the sliding surface in (12), this condition is given by

$$\dot{s} = k_d \ddot{e} + k_p \dot{e} + k_i e = 0 \tag{16}$$

The equivalent control is designed to ensure this condition holds for all t. Substituting $\ddot{e}$, in Eq. (16) produces

$$-\frac{k_\upsilon k_d}{m_\upsilon}\upsilon_1 - \frac{c_\upsilon k_d}{m_\upsilon}\upsilon_2 + \frac{k_d}{m_\upsilon}(u_{eq} + u_{sw}) + \frac{k_d}{m_\upsilon} d_\upsilon - k_d \ddot{\upsilon}_{1des} + k_p \dot{e} + k_i e = 0 \tag{17}$$

The equivalent control, u_{eq}, is selected as

$$u_{eq} = k_\upsilon \upsilon_1 + c_\upsilon \upsilon_2 - \hat{d}_\upsilon + m_\upsilon \ddot{\upsilon}_{1des} - \frac{m_\upsilon}{k_d}(k_p \dot{e} + k_i e) \tag{18}$$

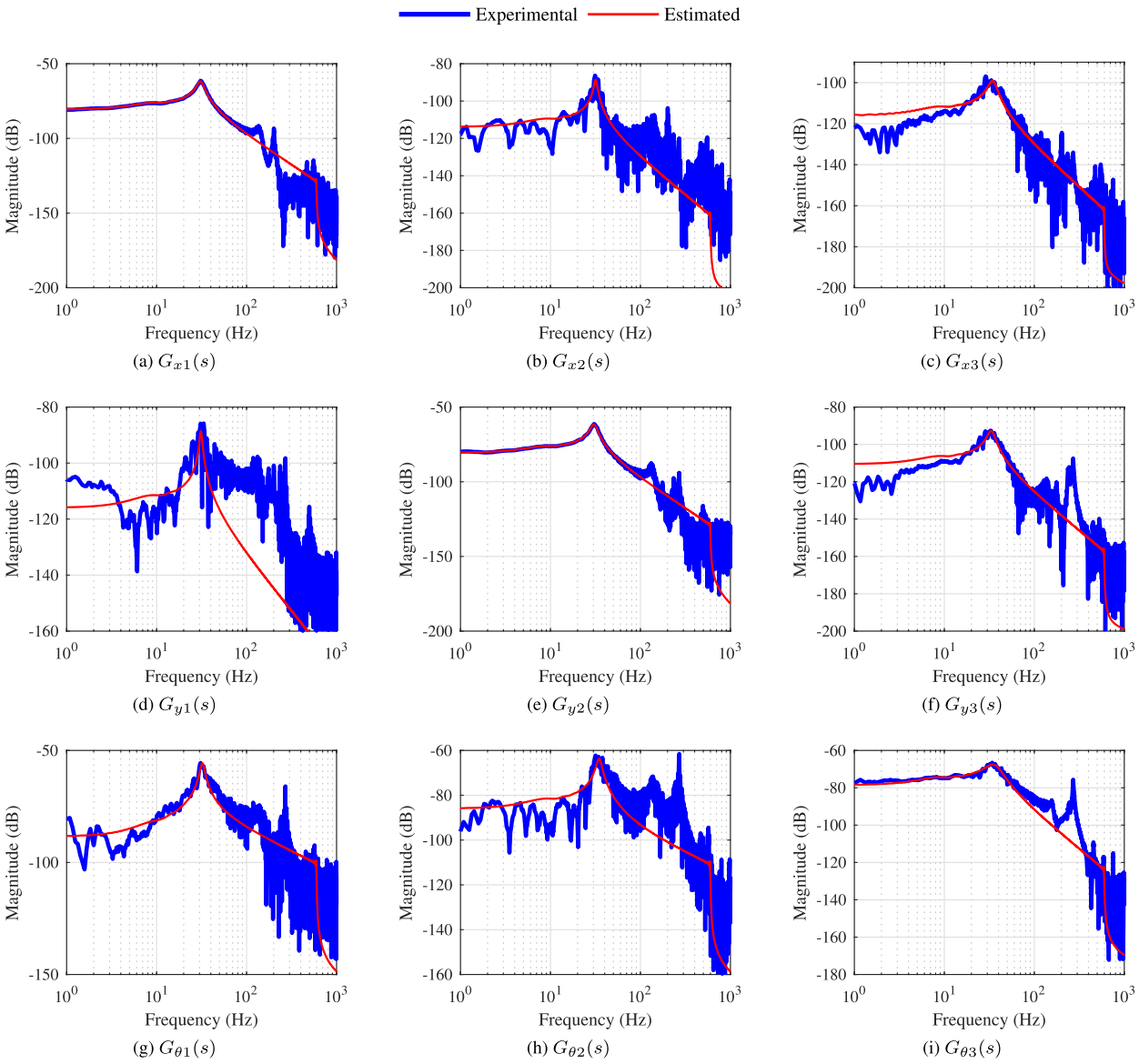

FIGURE 2. Experimental and estimated frequency response of the system.

where $\hat{d}_\upsilon(t)$ is the estimated disturbance. The system's stability is investigated using the following Lyapunov function

$$V_1 = \frac{s^2}{2} \tag{19}$$

The sliding surface is given by a liner PID equation, and it needs to be stable. Thus, it is sufficient to have non-negative PID gains to achieve a strictly Hurwitz system and hence the stability. Moreover, the overall stability and trajectories reachability to the sliding surface are guaranteed through

$$\dot{V}_1 = s\dot{s} \leq 0, \quad s \neq 0 \tag{20}$$

where Eq. (20) is called the reaching condition, and $\dot{V}_1$ is given by

$$\dot{V}_1 = s\frac{k_d}{m_\upsilon}(d_\upsilon - \hat{d}_\upsilon + u_{sw}) \tag{21}$$

The switching function is designed to preserve the stability of the system, and to achieve exponential reaching law to the sliding surface, as follows

$$u_{sw} = -k_1\, s - k_2 \text{sign}(s) \tag{22}$$

where $k_1, k_2 > 0$. Combining (22) with (21) gives

$$\dot{V}_1 = s\frac{k_d}{m_\upsilon}(\tilde{d}_\upsilon - k_1\, s - k_2 \text{sign}(s)) \tag{23}$$

where $\tilde{d}_\upsilon$ is the difference between the actual and estimated disturbance, and it is given by

$$\tilde{d}_\upsilon = d_\upsilon - \hat{d}_\upsilon \tag{24}$$

The reaching condition in Eq. (20), can be represented by

$$\begin{aligned} \dot{V}_1 &\leq -k_1 s^2 - k_2\,|s| + |\tilde{d}_\upsilon|\,|s| \leq 0 \\ &-k_1 s^2 - |s|\,(k_2 - |\tilde{d}_\upsilon|) \leq 0 \end{aligned} \tag{25}$$

This condition holds if k_2 is designed as

$$k_2 > |\tilde{d}_\upsilon| \tag{26}$$

It is worth noting that the stability of the system is determined by having the switching gain that is larger than the disturbance estimation error, rather than the disturbance bound itself. Thus, this reduction in gain bound will reduce the control signal chattering. The chattering phenomenon is strongly presented in the sliding mode control method due to the use of the signum function in the switching control. Chattering has an adverse effect on the safety of the actuators, and it is necessary to reduce its effect. Therefore the continuous function $\tanh(s/\epsilon)$ is used instead of $\text{sign}(s)$, where ϵ is a design parameter. It worth noting that when ϵ approaches zero, the tanh function approaches the signum one. The system stability with the $\tanh(s/\epsilon)$ function will be revisited in Section III-C.

B. NONLINEAR DISTURBANCE OBSERVER DESIGN

As explained earlier, the cross-coupling, VCM noise, uncertainty in parameters, etc. have a meaningful presence in the displacement of each axis. Therefore it is necessary to have an observer for estimation and compensation of those uncertainties. Nonlinear Disturbance Observer (NDO) has been proven to outperform linear observers for many systems studied in the literature [46], [47]. Thus it was adopted in this work. The state-space model in Eq. (10) is rewritten as

$$\dot{\upsilon} = f(\upsilon) + g_1(\upsilon)u_\upsilon + g_2(\upsilon)d_\upsilon \tag{27}$$

where

$$f(\upsilon) = \begin{bmatrix} \upsilon_2 \\ -\dfrac{k_\upsilon}{m_\upsilon}\upsilon_1 - \dfrac{c_\upsilon}{m_\upsilon}\upsilon_2 \end{bmatrix}, \quad g_1(\upsilon) = g_2(\upsilon) = \begin{bmatrix} 0 \\ \dfrac{1}{m_\upsilon} \end{bmatrix} \tag{28}$$

The NDO used for estimating d_υ is designed as

$$\hat{d}_\upsilon = z + p(\upsilon) \tag{29}$$

$$\dot{z} = -l(\upsilon)\left(g_2(\upsilon)\left(z + p(\upsilon)\right) + f(\upsilon) + g_1(\upsilon)u_\upsilon\right) \tag{30}$$

where $\hat{d}_\upsilon$ is the estimated disturbance, z is the observer's internal state, and $l(x)$ is the observer gain given by

$$l(\upsilon) = \frac{\partial p(\upsilon)}{\partial \upsilon} \tag{31}$$

Proposition 1: If it is assumed that disturbance dynamics changes slowly with time, and $p(\upsilon)$ is selected such that:

$$\dot{\tilde{d}}_\upsilon + \frac{\partial p(\upsilon)}{\partial \upsilon} g_2(\upsilon)\tilde{d}_\upsilon = 0 \tag{32}$$

then the estimated disturbance $\hat{d}_\upsilon$ approaches d_υ exponentially.

Proof: Selecting $p(\upsilon)$ as:

$$p(\upsilon) = k_3\upsilon_2 \tag{33}$$

therefore

$$l(\upsilon) = \frac{\partial p(\upsilon)}{\partial \upsilon} = \begin{bmatrix} 0 & k_3 \end{bmatrix} \tag{34}$$

and the observer dynamics is given by:

$$\dot{z} = -\frac{k_3}{m_\upsilon}\left(z - k_\upsilon\upsilon_1 + (k_3 - c_\upsilon)\upsilon_2 + u_\upsilon\right) \tag{35}$$

$$\hat{d}_\upsilon = z + k_3\upsilon_2 \tag{36}$$

differentiating Eq. (36) with respect to time gives:

$$\dot{\hat{d}}_\upsilon = \dot{z} + k_3\dot{\upsilon}_2 = \frac{k_3}{m_\upsilon}\left(d_\upsilon - \hat{d}_\upsilon\right) = \frac{k_3}{m_\upsilon}\tilde{d}_\upsilon \tag{37}$$

Differentiating Eq. (24) with respect to time and combining it with Eq. (37), results in:

$$\dot{\tilde{d}}_\upsilon + \frac{k_3}{m_\upsilon}\tilde{d}_\upsilon = 0 \tag{38}$$

which is equivalent to Eq. (32). It is worth noting that $\dot{d}_\upsilon = 0$ in Eq. (38) since it was assumed that d_υ varies slowly with time. The solution to differential equation given in Eq. (38) is found as

$$\tilde{d}_\upsilon = exp\left(-k_3/m_\upsilon t\right)\tilde{d}_\upsilon(t_0) \tag{39}$$

which converges to zero exponentially with time if $k_3 > 0$. ■

Proposition 2: If the single-axis dynamics given in Eq. (10) is considered with the NDO based sliding mode control approach proposed in Eqs. (18), (22), (35), and (36), then the overall system is stable and the control approach attracts the system's trajectories towards the sliding surface.

Proof: Finding a positive semi-definite Lyapunov function candidate, which involves trajectory tracking and disturbance estimation errors, is sufficient to prove this proposition. Thus, the following Lyapunov function is proposed:

$$V_2 = V_1 + \frac{\tilde{d}_\upsilon^{\,2}}{2} \tag{40}$$

differentiating Eq. (40) with respect to time gives:

$$\dot{V}_2 = \dot{V}_1 + \tilde{d}_\upsilon\dot{\tilde{d}}_\upsilon \tag{41}$$

$$= \dot{V}_1 - \frac{k_3}{m_\upsilon}\tilde{d}_\upsilon^{\,2} \tag{42}$$

$$\leq -k_1 s^2 - |s|\left(k_2 - |\tilde{d}_\upsilon|\right) - \frac{k_3}{m_\upsilon}\tilde{d}_\upsilon^{\,2} \leq 0 \tag{43}$$

which holds if the condition in Eq. (26) is satisfied. ■

The overall closed loop system block diagram is shown in Fig. 3, where the micropositioning system dynamics equation that is used in optimization and simulation is given by Eq. (11).

C. TIME CONVERGENCE ANALYSIS

The time convergence of the sliding function is investigated in this section when the disturbance observer, and chattering reduction methods are used. It follows from Eq. (42), with the substitution of $\tanh(s/\epsilon)$ in $\dot{V}_1$ for chattering reduction, the $\dot{V}_2$ is rewritten as:

$$\dot{V}_2 = s\frac{k_d}{m_\upsilon}\left(\tilde{d}_\upsilon - k_1 s - k_2\tanh(s/\epsilon)\right) - \frac{k_3}{m_\upsilon}\tilde{d}_\upsilon^{\,2} \tag{44}$$

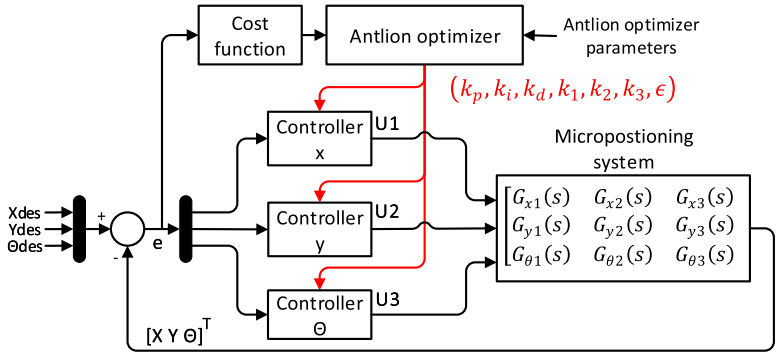

(a) Closed loop system block diagram

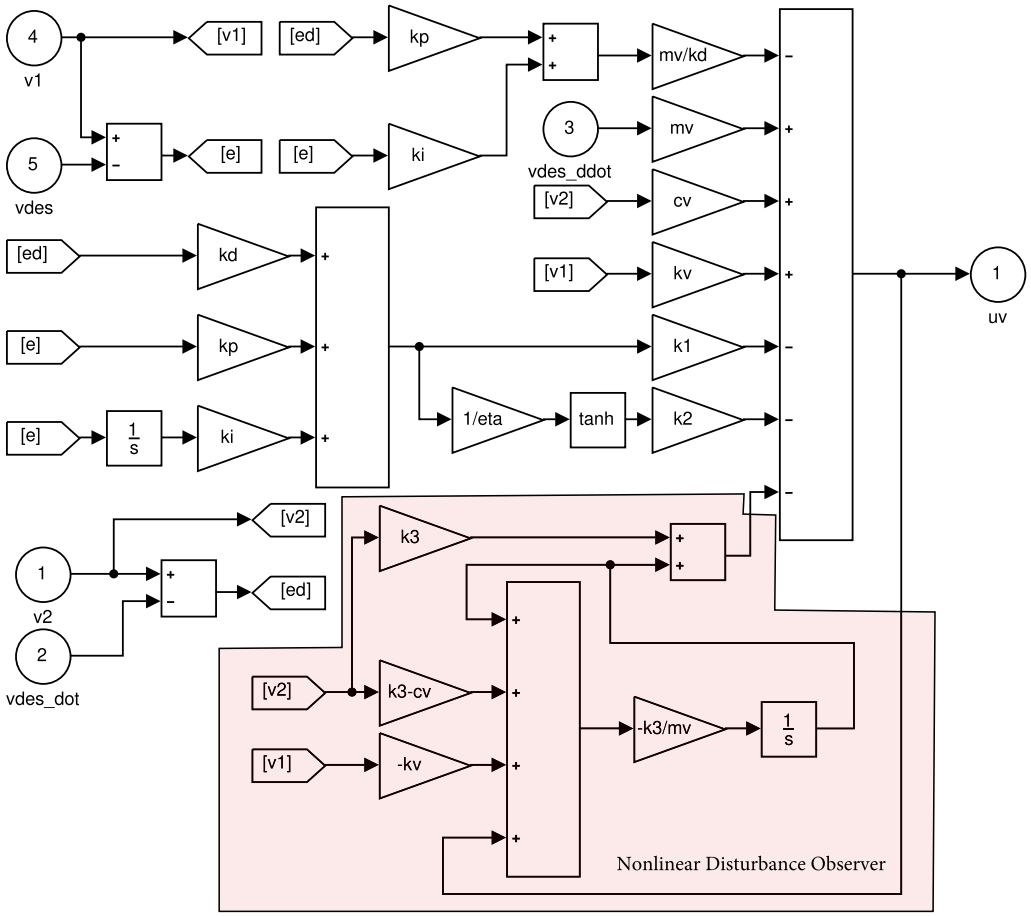

(b) SMC-NDO block diagram.

FIGURE 3. The overall closed loop system.

$$\dot{V}_2 \leq -k_1 s^2 - \frac{k_3}{m_\upsilon}\tilde{d}_\upsilon{}^2 + |s|\left|\tilde{d}_\upsilon\right| - k_2 s\tanh(s/\epsilon)$$
$$= -k_1 s^2 - \frac{k_3}{m_\upsilon}\tilde{d}_\upsilon{}^2 + |s|\left|\tilde{d}_\upsilon\right| - k_2|s| + k_2|s| - k_2 s\tanh(s/\epsilon) \quad (45)$$

Lemma 1 [48]: The following inequality holds $\forall\ \epsilon > 0$, $s \in \mathbb{R}$,

$$0 \leq |s| - s\tanh(s/\epsilon) \leq \delta\epsilon$$

where δ is a constant that satisfies $\delta = e^{-(\delta+1)}$, hence $\delta = 0.2785$.

Thus, Eq. (45) is written as:

$$\dot{V}_2 \leq -k_1 s^2 - \frac{k_3}{m_\upsilon}\tilde{d}_\upsilon{}^2 - |s|\left(k_2 - \left|\tilde{d}_\upsilon\right|\right) + k_2\delta\epsilon \quad (46)$$

with the consideration of the condition in Eq. (26), it can be found that

$$\dot{V}_2 \leq -k_1 s^2 - \frac{k_3}{m_\upsilon}\tilde{d}_\upsilon{}^2 + k_2\delta\epsilon \quad (47)$$

$$\dot{V}_2 \leq -\eta\left(\frac{s^2}{2}+\frac{\tilde{d_v}^2}{2}\right)+k_2\delta\epsilon \tag{48}$$

which is equivalent to:

$$\dot{V}_2 \leq -\eta V_2 + k_2\delta\epsilon \tag{49}$$

where $\eta = 2\min(k_1, k_3/m_v)$. The solution of Eq. (49) according to Lemma 2 is given by:

$$V_2(t) \leq \rho + (V_2(t_0)-\rho)\, e^{-\eta(t-t_0)} \tag{50}$$

where $\rho = k_2\delta\epsilon/\eta$, and it represents the maximum bound of the tracking error. Thus the sliding mode function is globally uniformly ultimately bounded. Moreover, the error bound ρ can be reduced by designing k_1, k_2, k_3, and ϵ.

Sliding mode chattering phenomena has a severe influence on the safety of the closed-loop system if not attenuated. Attenuation methods were proposed in the literature to reduce its impact. These methods cause the error to approach a given bound rather than zero. The parameters that affect this bound was not thoroughly identified and optimized in the literature towards optimal tracking. Thus, this bound (ρ) was theoretically derived in this section, and the parameters that affect it were established. These parameters are usually tuned in a try and error approach, which does not guarantee optimal performance. In this study, they are optimized to achieve better tracking performance and thus reducing ρ.

Lemma 2 [49]: Let $V, f : [0, \infty) \in \mathbb{R}$, if $\dot{V} \leq -\eta V + f$, $\forall t \geq t_0 \geq 0$, then $V(t)$ is bounded by the following function for any finite non-negative constant η

$$V(t) \leq e^{-\eta(t-t_0)}V(t_0) + \int_{t_0}^{t} e^{-\eta(t-\tau)}f(\tau)d\tau \tag{51}$$

Proof: Let $\mu(t) = \dot{V}(t) + \eta V(t) - f(t)$, where $\mu(t) < 0$, then:

$$\dot{V}(t) = -\eta V(t) + f(t) + \mu(t) \tag{52}$$

integrating Eq. (52) with respect to time gives:

$$V(t) = e^{-\eta(t-t_0)}V(t_0) + \int_{t_0}^{t} e^{-\eta(t-\tau)}f(\tau)d\tau + \int_{t_0}^{t} e^{-\eta(t-\tau)}\mu(\tau)d\tau \tag{53}$$

since $\mu(t) < 0$, then $\forall t \geq t_0 \geq 0$, it holds that:

$$V(t) \leq e^{-\eta(t-t_0)}V(t_0) + \int_{t_0}^{t} e^{-\eta(t-\tau)}f(\tau)d\tau \tag{54}$$

and that completes the proof. ■

IV. CONTROLLER OPTIMIZATION WITH ALO ALGORITHM

ALO mimics the foraging behavior of antlions during the larvae stage of their life cycle. Antlion excavates a funnel-shaped pit and hides at its bottom by coving itself with sand, as shown in Fig. 4. This pit forms a trap for ants that roam the area. Once an ant falls down the trap, it will find it difficult to escape due to the sharp edges of the trap. Then, antlion throughs sand on the trapped ant to prevent it from escape and to slide it down towards its jaws. Once the antlion captures its prey, it will consume it, and discard the remains. Then it will repair the pit and prepare it for the next hunting cycle.

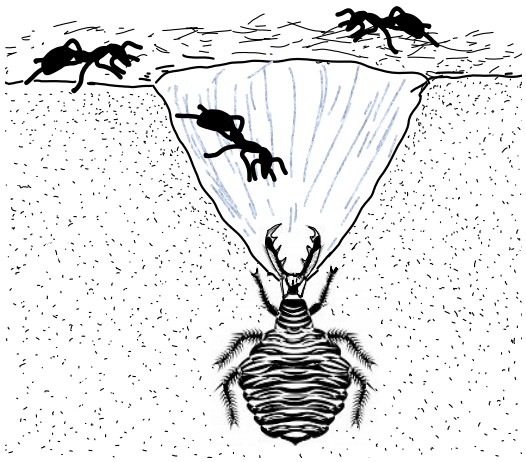

FIGURE 4. Antlion hunt mechanism.

ALO algorithm has two populations: antlions and ants, both collaborate to solve the optimization problem. The ants work as exploration agents in the solution space, while antlions disguise within the space, to capture the ants. Once an antlion captures a prey at a position, it would record that position, and hence it emerges as a fitter. The parameters of the problem represent the solution space dimensions, while ants positions refer to a particular solution within that space. The locations of ants and antlions are stored throughout the propagation of the algorithm as matrices. These matrices are used by ALO operators to converge towards the solution, and they are given by

$$\mathbf{M_{ant}} = \begin{bmatrix} Ant_{1,1} & Ant_{1,2} & \dots & Ant_{1,d} \\ Ant_{2,1} & Ant_{2,2} & \dots & Ant_{2,d} \\ \vdots & \vdots & \vdots & \vdots \\ Ant_{n,1} & Ant_{n,2} & \dots & Ant_{n,d} \end{bmatrix} \tag{55}$$

$$\mathbf{M_{antlion}} = \begin{bmatrix} AntL_{1,1} & AntL_{1,2} & \dots & AntL_{1,d} \\ AntL_{2,1} & AntL_{2,2} & \dots & AntL_{2,d} \\ \vdots & \vdots & \vdots & \vdots \\ AntL_{n,1} & AntL_{n,2} & \dots & AntL_{n,d} \end{bmatrix} \tag{56}$$

where d is the number of dimensions (number of parameters), and n is the number of ants/antlions. The locations of each ant and antlion are evaluated by an objective function f. Moreover, the fitnesses are found and stored for later use by the optimization processes. The fitness matrices are given by

$$\mathbf{M_{OFant}} = \begin{bmatrix} f\left(\left[Ant_{1,1},\ Ant_{1,2},\ \dots,\ Ant_{1,d}\right]\right) \\ f\left(\left[Ant_{2,1},\ Ant_{2,2},\ \dots,\ Ant_{2,d}\right]\right) \\ \vdots \\ f\left(\left[Ant_{n,1},\ Ant_{n,2},\ \dots,\ Ant_{n,d}\right]\right) \end{bmatrix} \tag{57}$$

$$\mathbf{M_{OFantlion}} = \begin{bmatrix} f\left(\left[AntL_{1,1},\ AntL_{1,2},\ \ldots,\ AntL_{1,d}\right]\right) \\ f\left(\left[AntL_{2,1},\ AntL_{2,2},\ \ldots,\ AntL_{2,d}\right]\right) \\ \vdots \\ f\left(\left[AntL_{n,1},\ AntL_{n,2},\ \ldots,\ AntL_{n,d}\right]\right) \end{bmatrix} \tag{58}$$

The following section describes the operations of ALO.

A. OPERATIONS OF ALO

The following operations are involved in the ALO.

1) RANDOM WALKS

The random walk of an ant in the i$^{\text{th}}$ dimension is described by:

$$X_i^k = \left[0,\ \sum_{j=1}^{1}(2r_j - 1),\ \sum_{j=1}^{2}(2r_j - 1),\ \ldots,\ \sum_{j=1}^{N_{iter}}(2r_j - 1)\right] \tag{59}$$

where N_{iter} is the maximum number of iterations, r is a random number described by:

$$r_j = \begin{cases} 1 & \text{if rand} > 0.5 \\ 0 & \text{if rand} \leq 0.5 \end{cases} \tag{60}$$

where rand is a uniformly distributed random number. Random walks are normalized to retain them within the search space using the following expression:

$$X_i^k|_{norm} = \frac{\left(X_i^k - a_i^k\right)\left(d_i^k - c_i^k\right)}{b_i^k - a_i^k} + c_i^k \tag{61}$$

where a_i^k, and b_i^k, are the minimum and maximum of the random walk X_i^k of the dimension i at the k$^{\text{th}}$ iteration, respectively. Moreover, c_i^k, and d_i^k are the upper and lower bounds of the i$^{\text{th}}$ dimension at the k$^{\text{th}}$ iteration.

2) ANTS TRAP IN PITS

The antlions traps affect the search space of ant, and that is modeled by

$$c_i^k = AntL_{j,i}^k + c_i^k \tag{62}$$

$$d_i^k = AntL_{j,i}^k + d_i^k \tag{63}$$

3) TRAPS BUILDING

The antlions are selected based on the roulette wheel selection method. The antlions with higher fitness will have a higher probability of being selected, and hence they participate in convergence towards the optimal solution.

4) ANTS SLIDING

When an ant is trapped in the antlion's pit, the antlion starts to throw sand grains on the ant to push it towards the bottom of the pit. This behavior is simulated by reducing the dimensions' boundaries adaptively as follows:

$$c_i^k = \frac{c_i^k}{I} \tag{64}$$

$$d_i^k = \frac{d_i^k}{I} \tag{65}$$

where I is an adaptive parameter that increases with the number of iteration, and it is given by:

$$I = \frac{10^w k}{N_{iter}} \tag{66}$$

w is given by:

$$w = \begin{cases} 2 & \text{if k} > 0.1N_{iter} \\ 3 & \text{if k} > 0.5N_{iter} \\ 4 & \text{if k} > 0.75N_{iter} \\ 5 & \text{if k} > 0.9N_{iter} \\ 6 & \text{if k} > 0.95N_{iter} \end{cases} \tag{67}$$

and it changes the accuracy of the solution with the iterations.

5) HUNTING A PREY AND AMENDING THE PIT

When the antlion hunts its prey, it will consume it. If the ant has better fitness than the antlion, the antlion will relocate itself to the position of the ant as follows

$$AntL_j^k = Ant_i^k \quad \text{if } f(Ant_i^k) > AntL_j^k \tag{68}$$

6) ELITISM

The best antlion in any iteration is selected as the elite one and kept for the next iteration. Thus, the best solution produced so far is preserved for the next iteration. The motion of the ants are updated by antlion selected from the roulette wheel, and the elite one, as follows

$$Ant_i^k = \frac{R_A^k + R_E^k}{2} \tag{69}$$

where R_A^k is a random walk of the i$^{\text{th}}$ ant around an antlion from the roulette wheel, similarly, the ant random walk around the elite antlion is given by R_E^k.

B. ALO ALGORITHM

The developed control approach requires the tuning of seven parameters in each axis (k_p, k_i, k_d, k_1, k_2, k_3, and ϵ), that means it is required to tune 21 parameters in total. Based on the operators presented in the previous section, the ALO algorithm for optimizing the developed robust controller in Section III is presented by Algorithm 1. The cost function is based on mean square error, and it is given by

$$cost = \frac{1}{n}\sum_{i=0}^{n}\left(e_x^2(i) + e_y^2(i) + e_\theta^2(i)\right) \tag{70}$$

Algorithm 1 ALO Algorithm for Optimizing Control Parameters

Require: cost function, parameters range, n, d, Niter
Result: A vector of optimized control parameters

```
Initialize the two populations randomly
Calculate the fitness using the objective function
stopCondition = False
while not stopCondition do
    for each ant do
        Use Roulette wheel to select an antlion
        Update the boundaries c and d using Eqs. (62), (63), (64), and (65)
        Create a normalized random walk using Eqs. (59), and (61)
        Update the ant's position using Eq. (69)
    end for
    Calculate the fitness of all ants using Eq. (70)
    Replace antlions with ants if they offer better fittness
    Update the elite antlion
    if (reached maximum iterations) or (reached a target fitness) then
        StopCondition = True
    end if
end while
Return the Elite antlion
```

where n is the number of simulation samples; e_x, e_y, and e_θ are the trajectory tracking error in x-, y-, and θ-axis, respectively. The number of ants are set to 25, and the number of iteration is selected as 100. The optimized parameters are given in Table 2. The cost function of the final iteration is 7.726e-13. The convergence curve of the optimization algorithm is shown in Fig. 5.

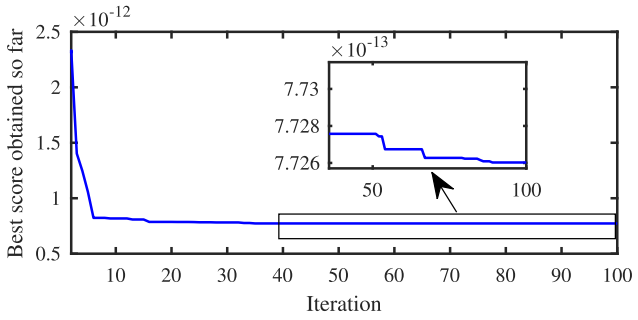

FIGURE 5. Cost function convergence curve.

V. EXPERIMENTAL RESULTS

The experimental setup of the system is shown in Fig. 6. It consists of three subsystems: optical system, electrical system, and mechanical system.

The optical system is based on Zygo laser-based displacement measurement system. It involves a laser head and three optical measurement paths. Each path measures a linear displacement for a point on the target stage using a laser interferometer. These three points are converted into two linear and one angular displacements. Three laser interferometers were used, two on the x-axis and one on the y-axis. The two x-axis interferometers are used to detect x and θ displacements, and the one on the y-axis is to detect y displacement only. Retroreflectors and external plane mirrors were used to reduce sensitivity to laser misalignment. The retroreflectors attached to the moving stage will reflect the incident beams in a parallel manner to off-stage plane mirrors, which in turn reflect them to the source. Then the laser beams travel through the optical components back to the interferometers to get finally picked up and transferred through the fibre optic cables to the measurement cards. Fold mirrors and beam splitters were used to facilitate laser beam steering from the laser head to the interferometers. The linear displacement measurements from the laser interferometers are converted in the software into two linear displacements (x and y), and one angular displacement (θ).

TABLE 2. Optimized controller and observer parameters.

Parameter	Lower bound	Upper bound	x-axis	y-axis	θ-axis
λ_0	0.5	1.5	0.519933774	1.33084289	0.5
λ_1	15	25	15.7645864	23.238396	25
λ_2	10e3	25e3	23928.0033	24383.2636	25000
k_1	1	3	2.97814911	2.88548827	2.49229754
k_2	0.1	1	0.19920302	0.790850786	0.943996182
k_3	5	15	14.249498	7.83774294	14.4285406
ϵ	0.1	1.5	0.642909385	0.605627841	0.1

The electrical system consists of Advantech PCI-1723 analog output data acquisition card, three VCMs VCAR0087-0062-00A, three LCAM 5/15 linear VCM drivers, and one unregulated DC power supply. The control action is supplied from the realtime software through the PCI-1723 as current commands to the VCM drivers. Each VCM driver has an internal closed-loop system to regulate the current in the VCM coil to the desired current command. The drivers require an unregulated power supply to function properly.

The mechanical system entails the 3-DOF micropositioner, VCM bases, mechanism base, and three studs to level the mechanism with the optical paths. The micropositioner was fabricated from Aluminum 7075-T6 and machined by wire electrical discharge machining technology for its high manufacturing precision.

The three systems were integrated into one feedback control system. An industrial PC deployed with Simulink realtime operating system was used to read the laser measurement and to send the VCM commands. Moreover, it also runs the control method, monitors, and records the signals. The sampling rate for the control experiment was selected as 5000 Hz, while for the system identification experiment, it was 10 kHz.

Several experiments were conducted to study the cross-coupling effect, and also to investigate the control approach performance in terms of resolution and trajectory tracking.

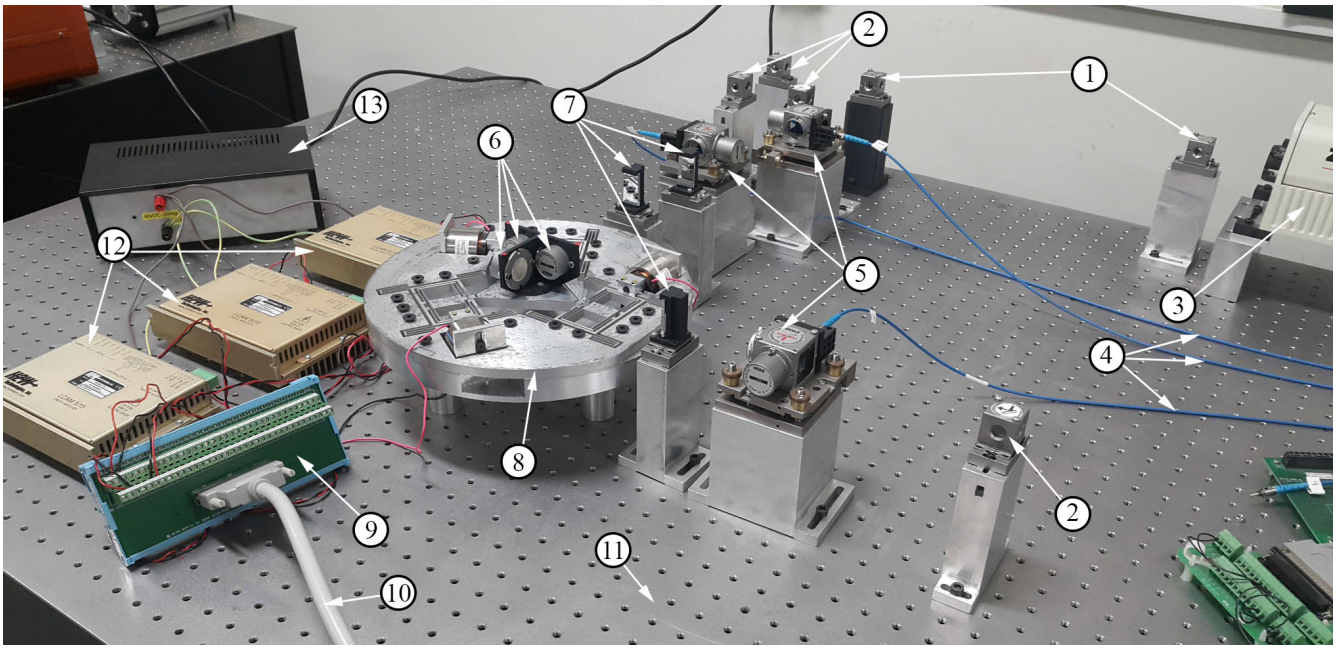

FIGURE 6. Experimental setup: (1) beam splitter, (2) fold mirror, (3) laser head, (4) fiber optic cable, (5) interferometer, (6) retroreflector, (7) plane mirror, (8) 3-DOF micropositioner, (9) Advantech PCI-1723 wiring terminal, (10) Advantech PCI-1723 extension cable, (11) vibration isolation optical table, (12) LCAM 5/15 VCM driver, (13) unregulated DC power supply.

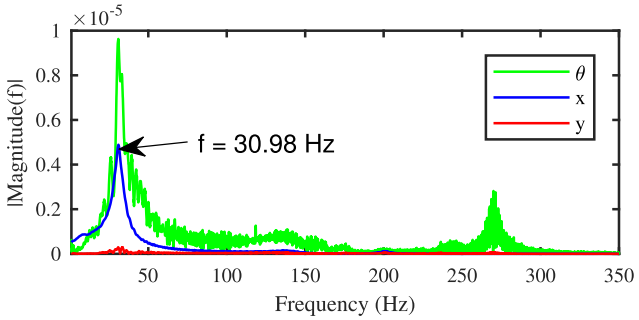

FIGURE 7. Single sided frequency spectrum for motion in x.

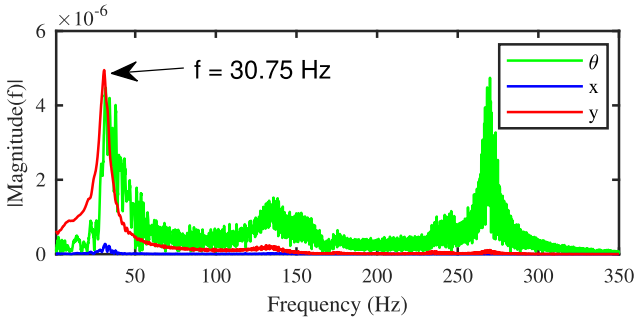

FIGURE 8. Single sided frequency spectrum for motion in y.

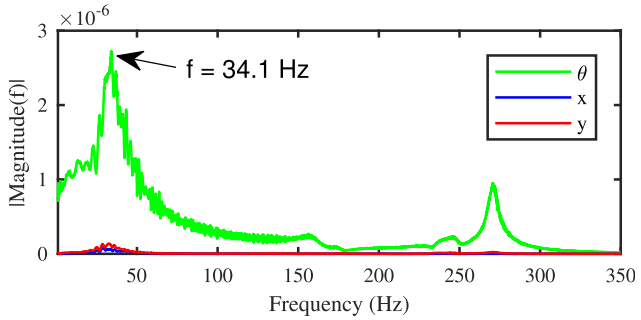

FIGURE 9. Single sided frequency spectrum for motion in θ.

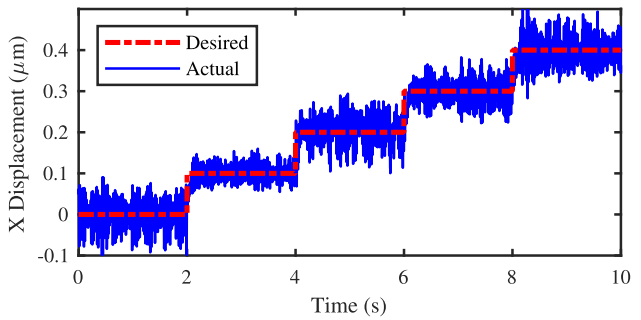

FIGURE 10. x-axis resolution.

A. CROSS-COUPLING EXPERIMENT

The single-sided frequency spectrum was utilized to show the impact of the cross-coupling near the resonant frequency. This spectrum can clearly show the amplitude and natural frequency of the intended motions and cross-couplings. The primary axes of motion were excited individually in open loop with the aid of inverse kinematics. A 0.1 V amplitude sinusoidal signal with a frequency spectrum from 1-350 Hz,

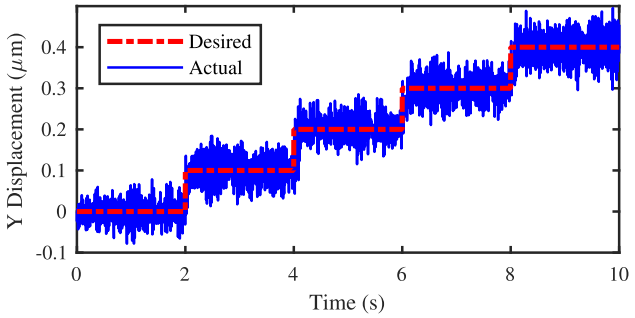

FIGURE 11. *y*-axis resolution.

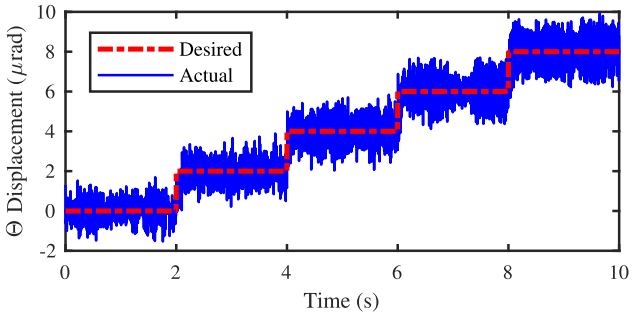

FIGURE 12. θ-axis resolution.

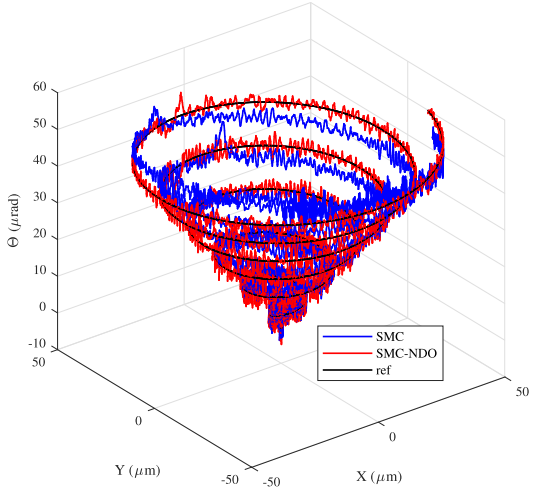

FIGURE 13. Whirlpool trajectory 3D plot.

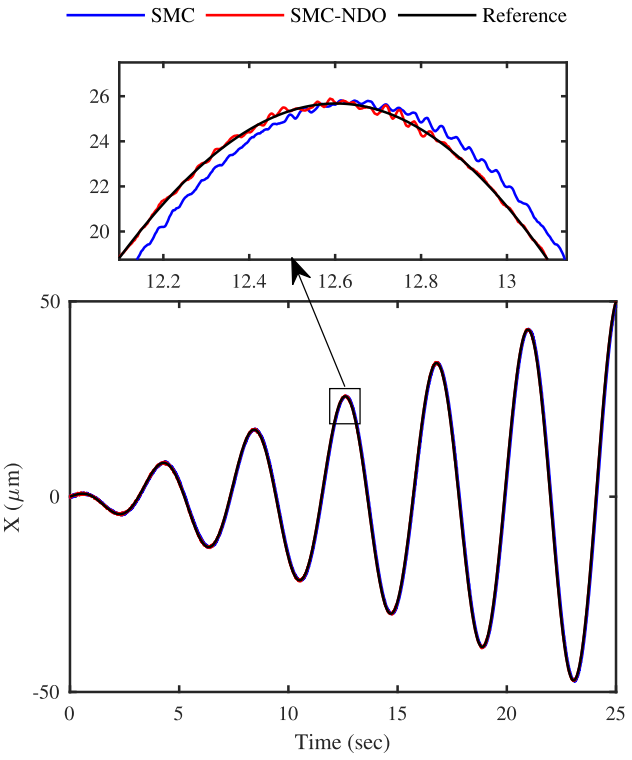

(a) x-axis tracking signal

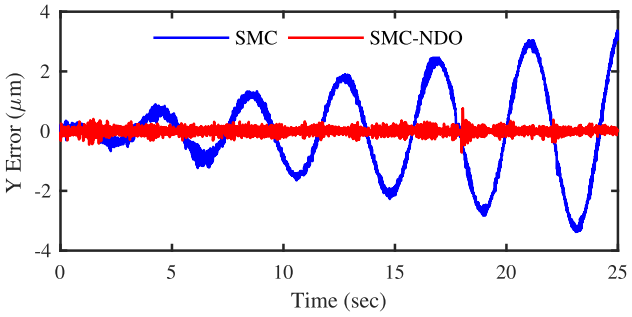

(b) x-axis tracking error

FIGURE 14. Whirlpool trajectory tracking of *x*-axis.

and a sampling frequency of 10 kHz was used as input to each axis in three open-loop experiments. The experimental time response data were recorded for each experiment. Then, the fast fourier transform is utilized to obtain the single-sided frequency spectrums with the aid of MATLAB. The severity of cross-coupling can be investigated through its magnitude near the resonant frequency of the primary axes. The single-sided frequency spectrums are shown in Figs. 7-9. It can be noticed that the cross-coupling from θ-axis exhibits a high magnitude at the resonance frequency of x- and y-axis. This indicates that the cross-coupling is interfering with the intended motions near the natural frequency and its effect should be attenuated.

In terms of natural frequencies, the intended motion of θ-axis appears slightly higher than the other two axes. However, the cross-coupling frequency of the θ-axis contaminates the intended motion of the other axes, as discussed earlier. The resonance frequency of the x-axis and y-axis are very close, which indicates the similar dynamics response in these two axes.

B. RESOLUTION TEST

The position resolution in the closed-loop scheme was experimentally investigated. A stair-step signal with 0.1 μm was used for testing the motion in both x and y axes, and 2 μrad was used to test the resolution of θ-axis. No overshoot was observed in the results due to the small step size. As shown

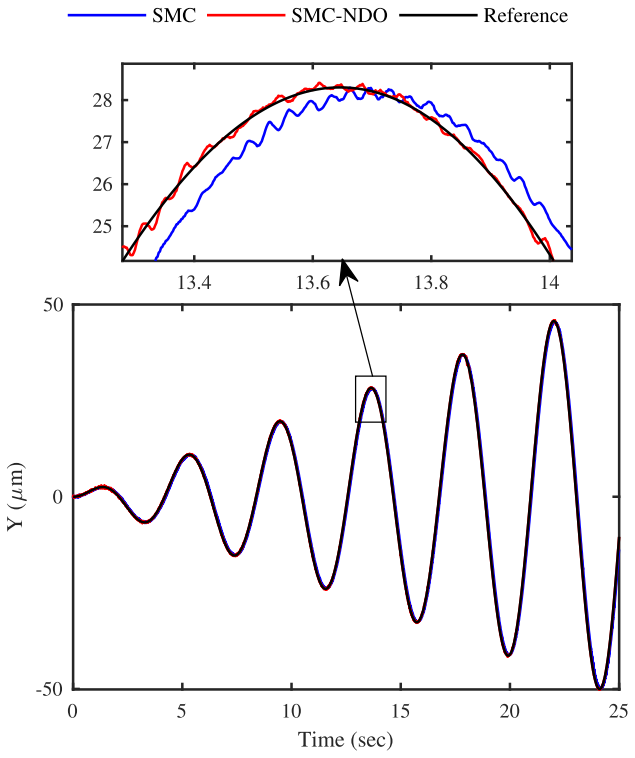

(a) y-axis tracking signal

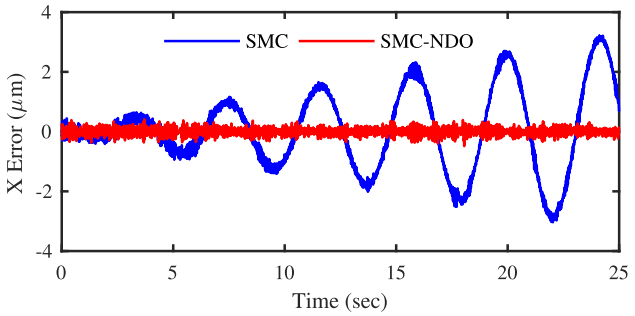

(b) y-axis tracking error

FIGURE 15. Whirlpool trajectory tracking of y-axis.

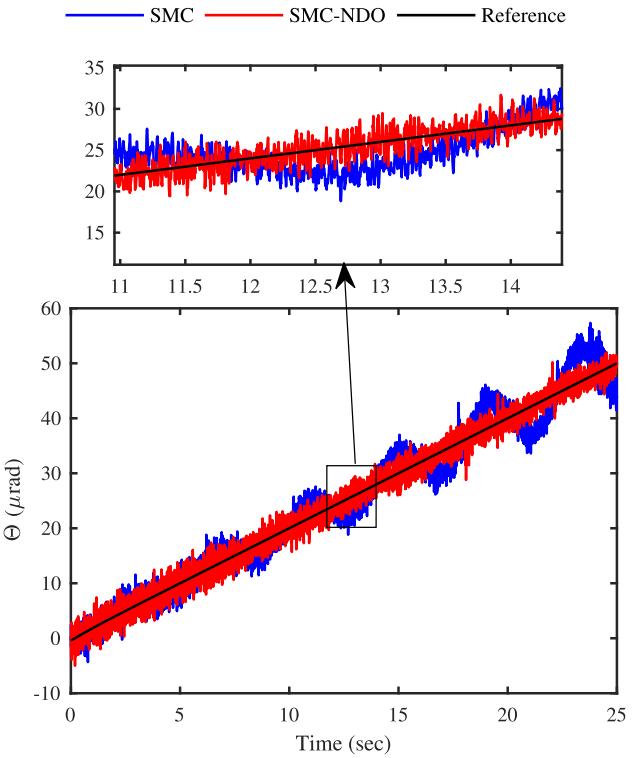

(a) θ-axis tracking signal

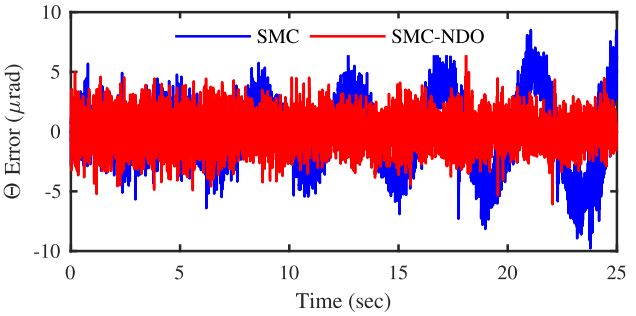

(b) θ-axis tracking error

FIGURE 16. Whirlpool trajectory tracking of θ-axis.

in Figs. 10-12, the control approach was able to resolve a resolution of 0.1 μm in x- and y-axis, and 2 μrad in θ-axis. It must be noted that resolution is sensitive to the noise level in the laser-based measurement system, VCM-coils, VCM-drivers, and analog channels of the data acquisition card. This represents a physical limitation to the resolution improvement.

C. TRAJECTORY TRACKING VALIDATION

A whirlpool 3-DOF trajectory was used to investigate the tracking performance when all the axes are simultaneously activated. The trajectory is described by

$$x_{ref} = 2t\cos(3t/2) \tag{71}$$

$$y_{ref} = 2t\sin(3t/2) \tag{72}$$

$$\theta_{ref} = 2t \tag{73}$$

where it has a diameter of 100 μm, and a height of 50 μrad when t reaches 25 s.

It can be seen from Fig. 14 and Fig. 15 that the SMC-NDO offers better tracking performance for both x and y axes than the classical SMC. As evident from Table 3, the SMC-NDO had improved the tracking by 91%, and 92%, for x- and y-axis, respectively. The error levels are comparable in the θ-axis as shown in Fig. 16, however, SMC-NDO was less sensitive to signal amplitude. The SMC-NDO achieved 49% improvement for θ-axis when compared with SMC. The control actions of the three axes are shown in Figs. 17-19. In these figures, the SMC-NDO exhibit higher control action than its counterparts as it provides disturbance compensation. Moreover, it was faster than the one from the SMC. Furthermore, the control signal for both methods showed less chattering due to the use of the tanh function.

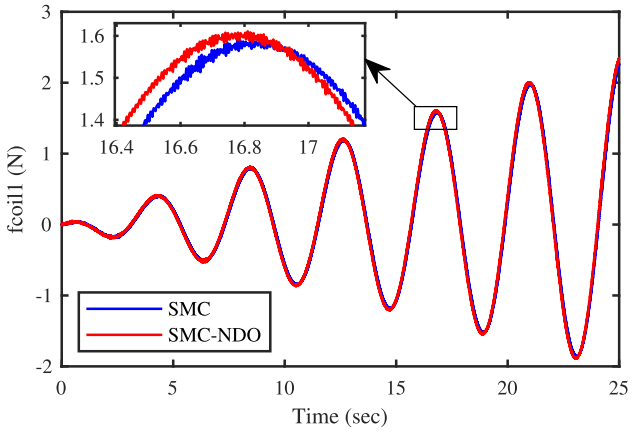

FIGURE 17. Control action to VCM 1.

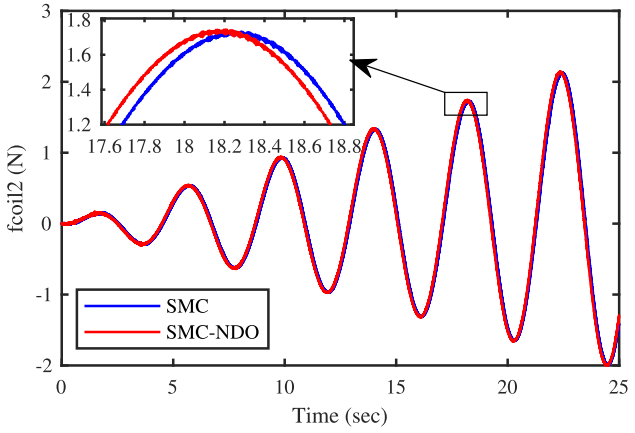

FIGURE 18. Control action to VCM 2.

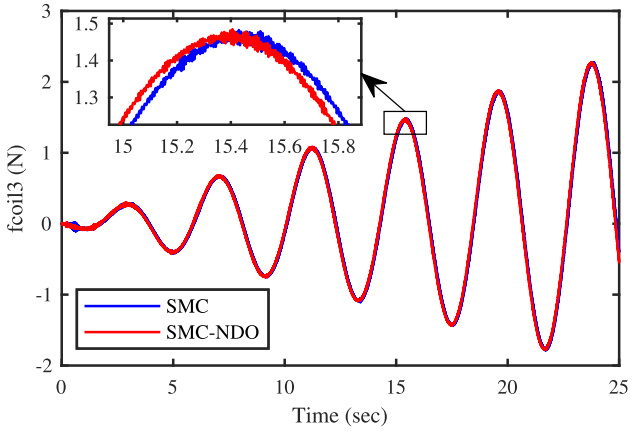

FIGURE 19. Control action to VCM 3.

The disturbance in mechanical systems can be estimated by rewriting Eq.(8), as follows [50]:

$$d_\upsilon(T) = m_\upsilon \ddot{\upsilon}(T) + c_\upsilon \dot{\upsilon}(T) + k_\upsilon \upsilon(T) - u_\upsilon(T-1) \quad (74)$$

However, this approach heavily depends on the sampling rate and the estimation accuracy of the acceleration signal,

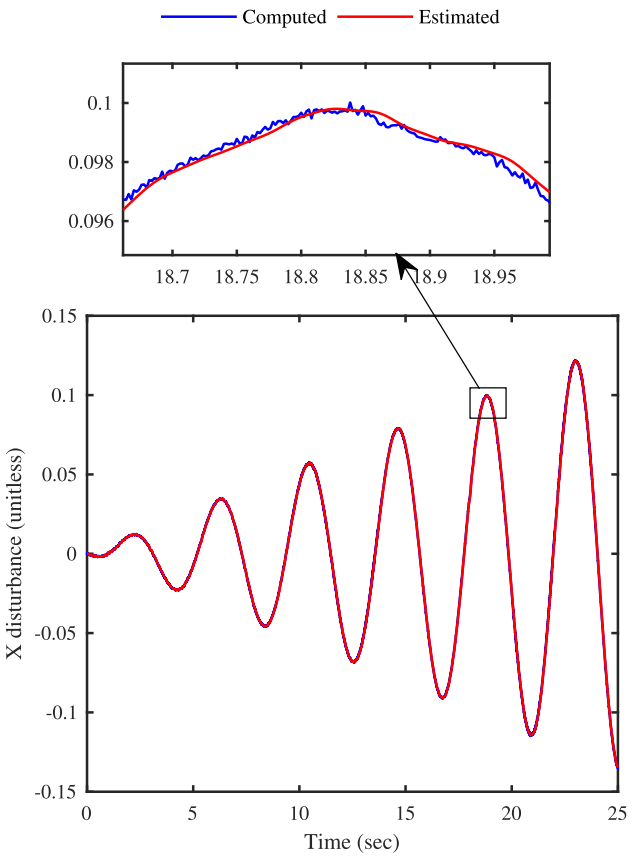

FIGURE 20. Disturbance estimation in x-axis.

which may not be practical for many systems. The estimated disturbance from the NDO was compared with the computed one given in Eq.(74). The acceleration signal in Eq.(74) was estimated using a digital differentiator with a low pass filter. The results are presented in Figs. 20-22. It can be noted from these results that the disturbance dynamics follow a similar shape of the reference signal. Moreover, the disturbance was changing slowly, which makes the assumption in Proposition 1 holds for all time. The disturbance estimated by the NDO was smother than the computed one, especially in θ-axis. That indicates the effectiveness of the NDO method.

Next, the accuracy of the simulated model was investigated in a comparative study with the experimental results. The SMC-NDO control method was utilized in the closed-loop feedback system, and the tracking error was used as a comparative index. The tracking errors of the simulated and experimental system are shown in Fig. 23. It can be noticed that the system's actual error levels were modeled accurately by the simulated system. However, the simulated system error signals were much smoother than the experimental ones. That is mainly ascribed to the noise accompanying the experimental system signals. Thus, the simulated system's error curves appeared almost matching the zero line, while the experimental system's error curves exhibited small fluctuations around that line.

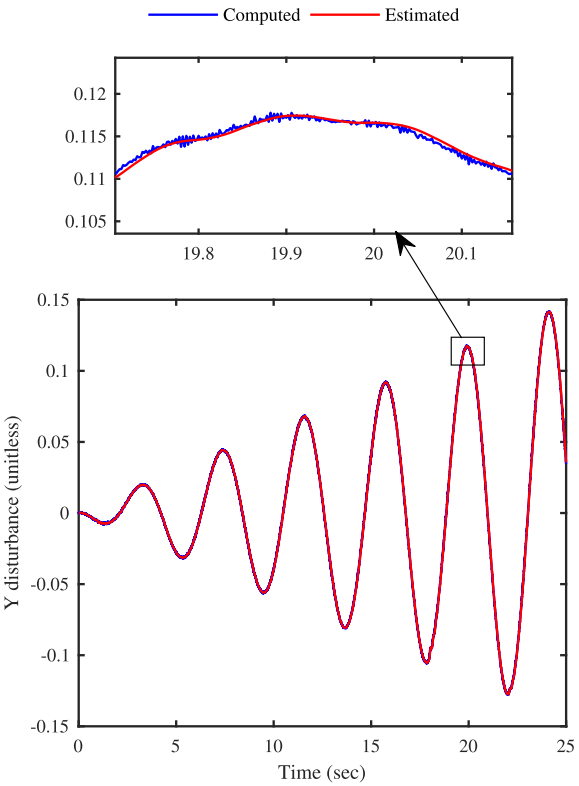

FIGURE 21. Disturbance estimation in y-axis.

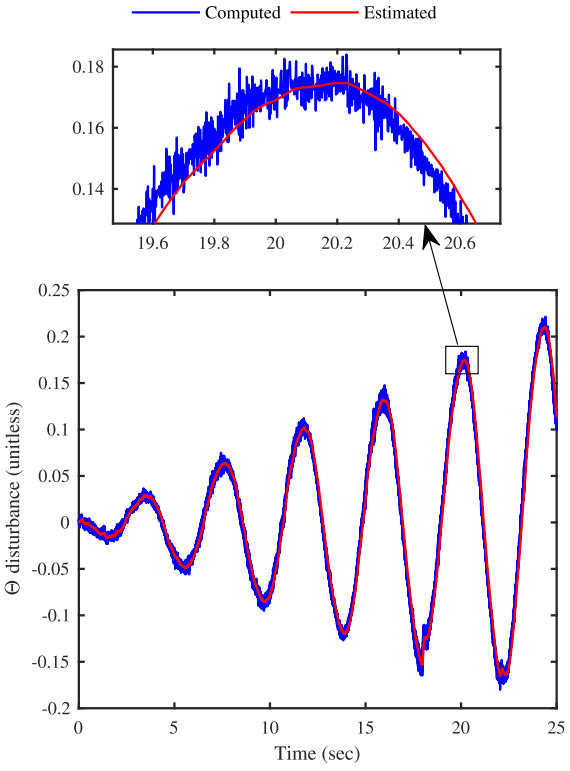

FIGURE 22. Disturbance estimation in θ-axis.

It can be concluded that the optimized control approach was able to provide high performance in both resolution and trajectory tracking experiments. Moreover, the cross-coupling effect is quite prominent in the tracking performance when the disturbance observer was not used. That was evident from the comparison of the SMC with the SMC-NDO. The SMC gains k_1 and k_2 were kept the same as in the SMC-NDO as increasing them resulted in oscillatory behavior of the mechanism. This can be attributed to the larger chattering that entered the system. This was avoided by the NDO as it estimates and compensates for the adverse effect of the cross-coupling disturbances without the need to have a larger controller gain. In fact, the use of the NDO reduced

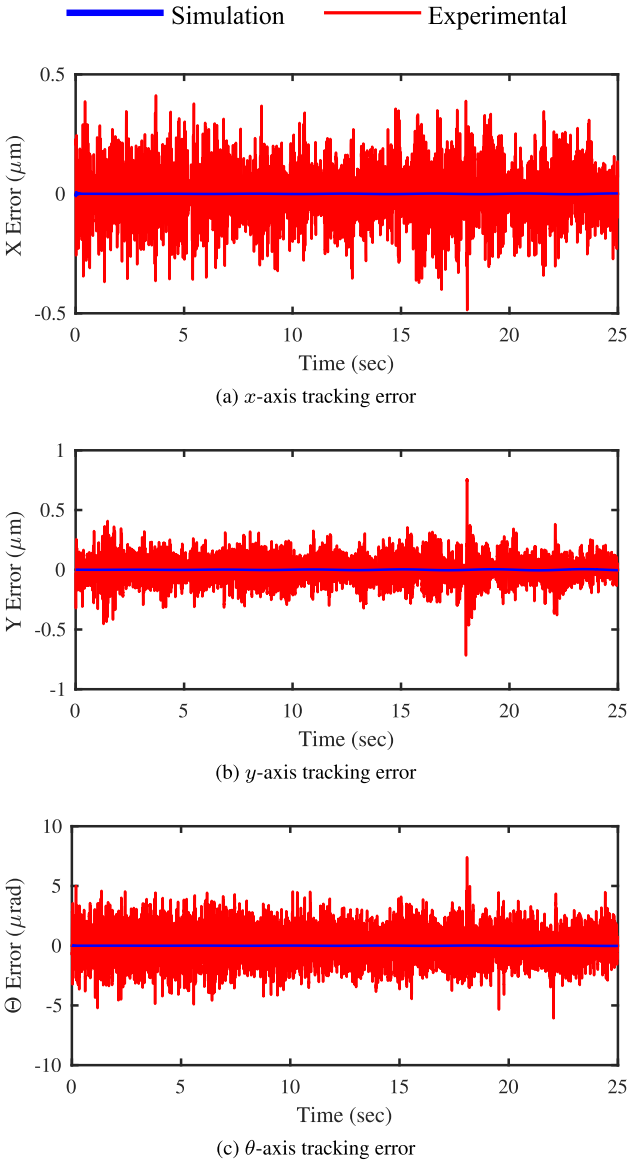

FIGURE 23. Simulated and experimental system tracking error when SMC-NDO was used.

TABLE 3. RMS error.

Axis	SMC RMSE (μ m)	SMC -NDO RMSE (μ m)
x	1.3448	0.1168
y	1.4187	0.1144
θ	2.8165	1.4265

the condition of having a gain that is larger than the bound of disturbance to a gain that is larger than the bound of the disturbance estimation error, which is much smaller. Thus the proposed method provides promising results for improving the tacking tasks of muti-DOF micro/nanopositioners.

VI. CONCLUSION

This paper presented the design, optimization, and analysis of a robust control technique for multi-DOF micropositioning. A nonlinear disturbance observer was merged with a sliding mode control approach to compensate the unavoidable cross-couplings presented in the system. Time convergence and stability analyses were performed to investigate the maximum tracking error and feedback stability, respectively. Manual tuning of a high number of controller parameters could result in suboptimal performance. Thus the antlion optimizer algorithm was used to automate the tuning process. Experimental results revealed that the developed control methodology provided better performance when compared with the classical sliding mode control, which is generally used for similar systems. Moreover, the experimental and simulated results were consistent, which indicates the accuracy of the modeling technique. The control method developed in this paper can be adopted to improve the tracking results for multi-DOF micro/nanopositioners that suffer from cross-coupling, parameter uncertainty, and disturbances. In future work, the proposed control method will be implemented to control coarse and fine motions in multi-DOF micropositioning stages.

APPENDIX A

Dynamic system transfer functions are given below

$$G_{x1}(s) = \frac{27.72}{s^2 + 32.86s + 3.772e04} \tag{75}$$

$$G_{x2}(s) = \frac{-4.933e-05s + 0.6427}{s^2 + 16.17s + 3.994e04} \tag{76}$$

$$G_{x3}(s) = \frac{0.6064}{s^2 + 47.24s + 4.778e04} \tag{77}$$

$$G_{y1}(s) = \frac{0.482}{s^2 + 12.45s + 3.814e04} \tag{78}$$

$$G_{y2}(s) = \frac{27.48}{s^2 + 32.29s + 3.693e04} \tag{79}$$

$$G_{y3}(s) = \frac{1.039}{s^2 + 40.68s + 4.42e04} \tag{80}$$

$$G_{\theta 1}(s) = \frac{0.1891s + 12.35}{s^2 + 22.54s + 4.11e04} \tag{81}$$

$$G_{\theta 2}(s) = \frac{-0.0573s - 19.17}{s^2 + 30.09s + 4.787e04} \tag{82}$$

$$G_{\theta 3}(s) = \frac{48.98}{s^2 + 97.96s + 5.215e04} \tag{83}$$

REFERENCES

[1] C. Lee, J. W. Lee, S. G. Ryu, and J. H. Oh, "Optimum design of a large area, flexure based XYΘ mask alignment stage for a 12-inch wafer using grey relation analysis," *Robot. Comput.-Integr. Manuf.*, vol. 58, pp. 109–119, Aug. 2019.

[2] J. Pinskier, B. Shirinzadeh, M. Ghafarian, T. K. Das, A. Al-Jodah, and R. Nowell, "Topology optimization of stiffness constrained flexure-hinges for precision and range maximization," *Mechanism Mach. Theory*, vol. 150, Aug. 2020, Art. no. 103874.

[3] J. Hesselbach, A. Raatz, and H. Kunzmann, "Performance of pseudo-elastic flexure hinges in parallel robots for micro-assembly tasks," *CIRP Ann.*, vol. 53, no. 1, pp. 329–332, 2004.

[4] G. Hao, X. Kong, and R. L. Reuben, "A nonlinear analysis of spatial compliant parallel modules: Multi-beam modules," *Mechanism Mach. Theory*, vol. 46, no. 5, pp. 680–706, May 2011.

[5] M. Yang, Z. Du, F. Chen, W. Dong, and D. Zhang, "Kinetostatic modelling of a 3-PRR planar compliant parallel manipulator with flexure pivots," *Precis. Eng.*, vol. 48, pp. 323–330, Apr. 2017.

[6] J. Zhu and G. Hao, "Design and test of a compact compliant gripper using the Scott–Russell mechanism," *Arch. Civil Mech. Eng.*, vol. 20, no. 3, pp. 0–12, Jun. 2020.

[7] G. Hao and J. Yu, "Design, modelling and analysis of a completely-decoupled XY compliant parallel manipulator," *Mechanism Mach. Theory*, vol. 102, pp. 179–195, Aug. 2016.

[8] J. Yu, Y. Xie, Z. Li, and G. Hao, "Design and experimental testing of an improved large-range decoupled XY compliant parallel micromanipulator1," *J. Mechnisms Robot.*, vol. 7, no. 4, p. 044503, Nov. 2015.

[9] C. Lee, C. K. Stepanick, S.-K. Lee, and J. A. Tarbutton, "Cross-coupling effect of large range XY nanopositioning stage fabricated by stereolithography process," *Precis. Eng.*, vol. 46, pp. 81–87, Oct. 2016.

[10] N. K. Roy and M. A. Cullinan, "Design and characterization of a two-axis, flexure-based nanopositioning stage with 50 mm travel and reduced higher order modes," *Precis. Eng.*, vol. 53, pp. 236–247, Jul. 2018.

[11] G. Hao and X. Kong, "A novel large-range XY compliant parallel manipulator with enhanced out-of-plane stiffness," *J. Mech. Des.*, vol. 134, no. 6, pp. 061009-1–061009-9, May 2012.

[12] R. Wang and X. Zhang, "A planar 3-DOF nanopositioning platform with large magnification," *Precis. Eng.*, vol. 46, pp. 221–231, Oct. 2016.

[13] Y. Zhang, P. Yan, and Z. Zhang, "A disturbance observer-based adaptive control approach for flexure beam nano manipulators," *ISA Trans.*, vol. 60, pp. 206–217, Jan. 2016.

[14] C. Li, C. Li, Z. Chen, and B. Yao, "Advanced synchronization control of a dual-linear-motor-driven gantry with rotational dynamics," *IEEE Trans. Ind. Electron.*, vol. 65, no. 9, pp. 7526–7535, Sep. 2018.

[15] Z. Chen, C. Li, B. Yao, M. Yuan, and C. Yang, "Integrated coordinated/synchronized contouring control of a dual-linear-motor-driven gantry," *IEEE Trans. Ind. Electron.*, vol. 67, no. 5, pp. 3944–3954, May 2020.

[16] D. Hwang, J. Byun, J. Jeong, and M. G. Lee, "Robust design and performance verification of an in-plane XYΘ micropositioning stage," *IEEE Trans. Nanotechnol.*, vol. 10, no. 6, pp. 1412–1423, Nov. 2011.

[17] G. Su, G. Lu, and P. Yan, "Planar motion measurement of a compliant micro stage: An enhanced microscopic vision approach," *IEEE Trans. Instrum. Meas.*, vol. 69, no. 5, pp. 1930–1939, May 2020.

[18] J. Y. Peng and X. B. Chen, "Integrated PID-based sliding mode state estimation and control for piezoelectric actuators," *IEEE/ASME Trans. Mechatronics*, vol. 19, no. 1, pp. 88–99, Feb. 2014.

[19] Q. Liu, J. Xiao, X. Yang, H. Liu, T. Huang, and D. G. Chetwynd, "An iterative tuning approach for feedforward control of parallel manipulators by considering joint couplings," *Mechanism Mach. Theory*, vol. 140, pp. 159–169, Oct. 2019.

[20] Z. Zhang, X. Yang, and P. Yan, "Large dynamic range tracking of an XY compliant nanomanipulator with cross-axis coupling reduction," *Mech. Syst. Signal Process.*, vol. 117, pp. 757–770, Feb. 2019.

[21] N. Wang and S.-F. Su, "Finite-time unknown observer-based interactive trajectory tracking control of asymmetric underactuated surface vehicles," *IEEE Trans. Control Syst. Technol.*, pp. 1–10, 2019.

[22] N. Wang and Z. Deng, "Finite-time fault estimator based fault-tolerance control for a surface vehicle with input saturations," *IEEE Trans. Ind. Informat.*, vol. 16, no. 2, pp. 1172–1181, Feb. 2020.

[23] N. Wang and H. He, "Dynamics-level finite-time fuzzy monocular visual servo of an unmanned surface vehicle," *IEEE Trans. Ind. Electron.*, vol. 67, no. 11, pp. 9648–9658, Nov. 2020.

[24] J. Yao and W. Deng, "Active disturbance rejection adaptive control of uncertain nonlinear systems: Theory and application," *Nonlinear Dyn.*, vol. 89, no. 3, pp. 1611–1624, May 2017.

[25] Q. Xu, "Adaptive integral terminal third-order finite-time sliding-mode strategy for robust nanopositioning control," *IEEE Trans. Ind. Electron.*, early access, Jun. 4, 2020, doi: 10.1109/TIE.2020.2998751.

[26] M. Acer and A. Şabanoviç, "Motion control of a redundant flexure based mechanism using piezoelectric actuators," *Automatika*, vol. 54, no. 1, pp. 114–125, Jan. 2013.
[27] S. Lu, C. Tian, and P. Yan, "Adaptive extended state observer-based synergetic control for a long-stroke compliant microstage with stress stiffening," *IEEE/ASME Trans. Mechatronics*, vol. 25, no. 1, pp. 259–270, Feb. 2020.
[28] M. Mitchell, *An Introduction to Genetic Algorithms*. Cambridge, MA, USA: MIT Press, 1998.
[29] K. Price, R. M. Storn, and J. A. Lampinen, *Differential Evolution: A Practical Approach to Global Optimization* (Natural Computing Series). Berlin, Germany: Springer-Verlag, 2005.
[30] J. Kennedy and R. Eberhart, "Particle swarm optimization," in *Proc. IEEE ICNN*, vol. 4, Nov./Dec. 1995, pp. 1942–1948.
[31] A. A. Al-Azza, A. A. Al-Jodah, and F. J. Harackiewicz, "Spider monkey optimization: A novel technique for antenna optimization," *IEEE Antennas Wireless Propag. Lett.*, vol. 15, pp. 1016–1019, 2016.
[32] S. Mirjalili, "The ant lion optimizer," *Adv. Eng. Softw.*, vol. 83, pp. 80–98, May 2015.
[33] A. Fathy and A. M. Kassem, "Antlion optimizer-ANFIS load frequency control for multi-interconnected plants comprising photovoltaic and wind turbine," *ISA Trans.*, vol. 87, pp. 282–296, Apr. 2019.
[34] H. Kılıç and U. Yüzgeç, "Improved antlion optimization algorithm via tournament selection and its application to parallel machine scheduling," *Comput. Ind. Eng.*, vol. 132, pp. 166–186, Jun. 2019.
[35] S. Dalwinder, S. Birmohan, and K. Manpreet, "Simultaneous feature weighting and parameter determination of neural networks using ant lion optimization for the classification of breast cancer," *Biocybernetics Biomed. Eng.*, vol. 40, no. 1, pp. 337–351, Jan. 2020.
[36] M. A. Ebrahim, M. N. Ahmed, H. S. Ramadan, M. Becherif, and J. Zhao, "Optimal Metaheuristic-based sliding mode control of VSC-HVDC transmission systems," *Math. Comput. Simul.*, vol. 179, pp. 178–193, Jan. 2021.
[37] W. Boukadida, A. Benamor, H. Messaoud, and P. Siarry, "Multi-objective design of optimal higher order sliding mode control for robust tracking of 2-DoF helicopter system based on metaheuristics," *Aerosp. Sci. Technol.*, vol. 91, pp. 442–455, Aug. 2019.
[38] J. Oliveira, P. M. Oliveira, J. Boaventura-Cunha, and T. Pinho, "Chaos-based grey wolf optimizer for higher order sliding mode position control of a robotic manipulator," *Nonlinear Dyn.*, vol. 90, no. 2, pp. 1353–1362, Aug. 2017.
[39] Q. Xu, "Design, testing and precision control of a novel long-stroke flexure micropositioning system," *Mechanism Mach. Theory*, vol. 70, pp. 209–224, Dec. 2013.
[40] A. Al-Jodah, B. Shirinzadeh, M. Ghafarian, Y. Tian, and L. Clark, "Design and analysis of a novel 3-DOF large range micropositioning mechanism," in *Proc. IEEE/ASME Int. Conf. Adv. Intell. Mechatronics (AIM)*, Jul. 2018, pp. 991–996.
[41] Y.-M. Choi, J. J. Kim, J. Kim, and D.-G. Gweon, "Design and control of a nanoprecision XYΘ scanner," *Rev. Sci. Instrum.*, vol. 79, no. 4, Apr. 2008, Art. no. 045109.
[42] J. Pinskier, B. Shirinzadeh, L. Clark, and Y. Qin, "Development of a 4-DOF haptic micromanipulator utilizing a hybrid parallel-serial flexure mechanism," *Mechatronics*, vol. 50, pp. 55–68, Apr. 2018.
[43] A. Al-Jodah, B. Shirinzadeh, M. Ghafarian, T. Kumar Das, Y. Tian, and D. Zhang, "A fuzzy disturbance observer based control approach for a novel 1-DOF micropositioning mechanism," *Mechatronics*, vol. 65, Feb. 2020, Art. no. 102317.
[44] S. Yu, X. Yu, B. Shirinzadeh, and Z. Man, "Continuous finite-time control for robotic manipulators with terminal sliding mode," *Automatica*, vol. 41, no. 11, pp. 1957–1964, Nov. 2005.
[45] M. Ghafarian, B. Shirinzadeh, A. Al-Jodah, and T. K. Das, "Adaptive fuzzy sliding mode control for high-precision motion tracking of a multi-DOF Micro/Nano manipulator," *IEEE Robot. Autom. Lett.*, vol. 5, no. 3, pp. 4313–4320, Jul. 2020.
[46] W.-H. Chen, D. J. Ballance, P. J. Gawthrop, and J. O'Reilly, "A nonlinear disturbance observer for robotic manipulators," *IEEE Trans. Ind. Electron.*, vol. 47, no. 4, pp. 932–938, Aug. 2000.
[47] W.-H. Chen, "Nonlinear disturbance observer-enhanced dynamic inversion control of missiles," *J. Guid., Control, Dyn.*, vol. 26, no. 1, pp. 161–166, Jan. 2003.
[48] M. M. Polycarpou and P. A. Ioannou, "A robust adaptive nonlinear control design," *Automatica*, vol. 32, no. 3, pp. 423–427, Mar. 1996.
[49] P. Ioannou and J. Sun, *Robust Adaptive Control* (Control Theory), vol. 1. Upper Saddle River, NJ, USA: Prentice-Hall, 1996.
[50] H. Elmali and N. Olgac, "Implementation of sliding mode control with perturbation estimation (SMCPE)," *IEEE Trans. Control Syst. Technol.*, vol. 4, no. 1, pp. 79–85, Jan. 1996.

AMMAR AL-JODAH (Graduate Student Member, IEEE) received the B.Sc. degree in control and systems engineering from the University of Technology, Iraq, and the M.Sc. degree in electrical and computer engineering from Southern Illinois University, Carbondale, USA. He is currently pursuing the Ph.D. degree with the Robotics and Mechatronics Research Laboratory, Monash University, Australia. His research interests include large range micro/nanomanipulation mechanisms, laser interferometry-based measurement systems, robust controller design, and real-time controllers.

BIJAN SHIRINZADEH (Member, IEEE) received the B.Eng. degree in mechanical engineering, the B.Eng. degree in aerospace engineering, and the M.S.Eng. degree in mechanical engineering from the University of Michigan, Ann Arbor, and the Ph.D. degree in mechanical engineering from The University of Western Australia (UWA). He is currently a Full Professor and the Director of the Robotics and Mechatronics Research Laboratory (RMRL). His current research interests include laser-based measurements and sensory-based control, micro/nanomanipulation mechanisms and systems, serial and parallel mechanisms, and automated manufacturing.

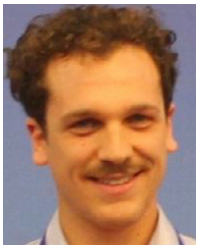

JOSHUA PINSKIER (Member, IEEE) received the Ph.D. degree in mechanical engineering from Monash University, Melbourne, Australia, in 2019. He is currently working as a Postdoctoral Researcher with the Robotics and Mechatronics Research Laboratory, Monash University. His research interests include micro/nanomanipulation systems, teleoperation, flexure-mechanism design, biological-cell handling, and real-time control.

MOHAMMADALI GHAFARIAN (Graduate Student Member, IEEE) received the B.E. and M.E. degrees in Iran, in 2011 and 2014, respectively. He is currently pursuing the Ph.D. degree in micro/nanomanipulation with the Robotics and Mechatronics Research Laboratory (RMRL). His current research interests include micro/nanomanipulation mechanisms, control methodology, piezoelectric actuators, and vibration.

TILOK KUMAR DAS (Graduate Student Member, IEEE) received the B.Sc. degree in mechanical engineering from the Chittagong University of Engineering and Technology and the M.Eng. degree in mechanical and space engineering from Hokkaido University. He is currently pursuing the Ph.D. degree with the micro/nanomanipulation with the Robotics and Mechatronics Research Laboratory (RMRL). His research interests include micro/nanomanipulation systems, end-effectors, and real-time control.

YANLING TIAN received the Ph.D. degree in mechanical engineering from Tianjin University, China. He was a Postdoctoral Research Officer with the Robotics and Mechatronics Research Laboratory, Department of Mechanical and Aerospace Engineering, Monash University, Australia. He is currently a Professor with Tianjin University, China. His research interests include micro/nanomanipulation, mechanical dynamics, surface metrology, and characterization.

DAWEI ZHANG received the B.Eng. degree in mechanical engineering from the Shenyang University of Technology, Shenyang, China, in 1984, and the M.Sc. and Ph.D. degrees in mechanical engineering from Tianjin University, Tianjin, China, in 1990 and 1995, respectively. From 1984 to 1987, he was an Associate Engineer with the Tianjin Institute of Power Source, China. He is currently a Professor with the School of Mechanical Engineering, Tianjin University. His current research interests include micro/nanopositioning technique, structural dynamics, signal processing, high-speed machining methodologies, and dynamic design of machine tools.